Research Article

Enhancing flat plate collectors' efficiency by minimizing optical losses through vacuum glazing and ethylene glycol-diamond-alumina nanofluid

Muhammad SHEHRAM[1] , **Muhammad Najwan HAMIDI**[1,*] , **Aeizaal Azman A. WAHAB**[1] ,
M. K. Mat DESA[1]

[1]School of Electrical and Electronic Engineering, Universiti Sains Malaysia, Pulau Pinang, 14300, Malaysia

ABSTRACT

This study addresses the critical need to improve the efficiency of solar flat plate collectors (FPC) where the key factors influencing their performance include the choice of working fluids, exposure to sunlight, and minimizing heat loss. Carbon-based nanofluids, known for their exceptional thermal stability and heat transfer properties, emerge as a promising solution. This research presents an innovative approach by combining carbon-based (ethylene glycol-diamond) and metal-oxide-based (alumina) hybrid nanofluids to boost collector efficiency. Additionally, a two-step strategy is employed to reduce reflection losses. A triple glaze is applied to the collector's top surface, followed by vacuum glazing. The latter, consisting of three layers of low-iron glass with an emissivity of 0.20 and a solar transmittance of 0.87 which reduces the glass thickness. This integration of vacuum glass and hybrid nanofluid results in an 82% increase in FPC efficiency. The nanofluids, with nanoparticles sized between 100 and 200 nm and material volume fractions of 0.3% for carbon-based and 0.1% for metal-oxide-based components, circulate at 4 L/min. Ethylene glycol has an energy efficiency of 58%, alumina 68%, and diamond nanofluids 71.8%. Heat transfer coefficients are 0.88 for ethylene glycol, 0.93 for alumina-based nanofluids, and 0.98 for diamond-based fluid. The hybrid nanofluids also exhibit heat loss ranging from 2.4 W/m.K to 4.0 W/m.K. Triple glaze vacuum layers achieve an efficiency peak of 82%, significantly reducing heat loss to 700W compared to single and double layers. The study utilizes Python in an Anaconda Jupyter notebook for detailed system modeling, facilitating thorough simulation of the system.

Cite this article as: Shehram M, Hamidi MN, Wahab AAA, Desa MKM. Enhancing flat plate collectors' efficiency by minimizing optical losses through vacuum glazing and ethylene glycol-diamond-alumina nanofluid. J Ther Eng 2025;11(2):550–576.

INTRODUCTION

Today, the need for energy is on the rise, and meeting this demand relies heavily on costly energy sources, such as fossil fuels and petroleum. Solar energy is the most promising solution to address this energy demand. Solar thermal collectors play a pivotal role in harnessing the thermal radiation from the sun and serve as energy sources. However,

*Corresponding author.
*E-mail address: najwan@usm.my

This paper was recommended for publication in revised form by Editor-in-Chief Ahmet Selim Dalkılıç

a significant portion of thermal energy is wasted owing to various factors, including collector performance, optical losses, and the characteristics of the fluid used. To enhance the efficiency of thermal collectors, ongoing research is dedicated to developing innovative heat transfer fluids and improving the thermal collector design.

In [1], the FPC efficiency was significantly improved with hybrid nanofluids engineered for better thermal heat absorption. These nanofluids come in various formulations, including metal-based and metal-oxide-based options, enhancing heat-transfer fluids with impressive thermal conductivity. The research focuses on graphene-silicon and water-based hybrid nanofluids for FPCs, offering notably higher thermal conductivity and concentration ratios than previous nanofluids [2]. Two distinct hybrid nanofluids, blended with pure water, were used to optimize thermal energy extraction from FPCs [3]. Turbulence-inducing agents boost the heat transfer rates in combination with distilled water to enhance efficiency. Material concentration ratios of 0.01%, 0.05%, and 0.1% by weight improved the FPC performance compared with the current system [4].

Alumina (Al_2O_3) water-based nanofluids, containing 20 nm particles at a volume of 0.1%, boost the FPC efficiency by 23.6% at a 2 L/min flow rate [5]. In [6], zinc oxide (ZnO) and copper oxide (CuO) water-based nanofluids with 0.15% volume fraction achieved an efficiency increase of 77.64% at a flow rate of 0.0125 kg/s. Fe_2O_4/water-based nanofluids with a 0.5% particle concentration enhanced collector efficiency by 6.6%, aided by MATLAB coding for thermal calculations [7]. Meanwhile, cerium oxide (CeO_2)-water-based nanofluids with particle volume fractions of 0.0167%, 0.0333%, and 0.066% and 25 nm particle size enhance the thermal collector efficiency by 10.74% [8]. These nanofluid compositions demonstrated significant improvements in FPC performance.

A blend of alumina (Al_2O_3) and titanium oxide (TiO_2) nanofluids, each at a 0.1% weight ratio, featuring 20 nm and 15 nm particle sizes, respectively, increased the collector thermal efficiency to 19-21% [9]. Titanium oxide in water nanofluids alone achieved a collector efficiency of 78% and an improvement of 9.80%. These gains depend on the sunlight intensity and the inlet-outlet temperature difference [10]. In [11], a 0.5% ratio of alumina and crystal nanocellulose nanofluids boosts the solar thermal collector efficiency by 2.8-8.46%, with viscosity inversely related to temperature. Hybrid nanofluids exhibit strong thermal conductivity, with copper-copper oxide (Cu-CuO)/water nanofluids increasing the collector conductivity by 17.52% and exergy efficiency by 2.3% [12]. These nanofluids offer substantial enhancements in the collector performance.

The performance of thermal collectors was evaluated based on energy and exergy parameters, employing four types of nanofluids: alumina (Al_2O_3)/water, magnesium (Mg)/water, titanium (Ti)/water, and copper oxide (CuO)/water, all operated at flow rates ranging from 1 to 4 L/min [13]. Efficiency was found to increase with higher fluid

density. Additionally, the effectiveness of graphene-based nanofluids was examined under sunlight intensities of 600 W/m^2, 800 W/m^2, and 1000 W/m^2, with mass flow rates ranging from 1.2 to 1.5 L/min, resulting in a potential efficiency enhancement of up to 7.9% [14]. Another study explored the use of graphene and crystal nano-cellulose nanofluids, with concentrations ranging from 0.3% to 0.5% and a volumetric fraction of 0.5%, to improve collector performance [15]. Furthermore, the utilization of copper oxide nanofluids in distilled water was found to enhance thermal performance by up to 4% across various temperatures, simultaneously reducing pressure while augmenting energy transfer and heat gain for FPCs [16]. Table 1 provides a comparative analysis of the properties of the various nanofluid types. There are two primary categories of nanofluids: metal-based and carbon-based, with metal oxide being another form. Carbon-based nanofluids exhibit superior thermal conductivity and heat-bearing capacity when compared to other nanoparticles. Metal-based nanofluids also demonstrate commendable thermal conductivity and volume fraction. In contrast, metal-oxide-based nanofluids generally possess lower thermal conductivity compared to carbon-based and metal-based nanofluids [17].

For FPCs, low-emissivity coatings on glass materials reduce optical losses. Selective glass layers, such as tin-doped indium oxide and aluminium-doped zinc oxide, minimize reflection loss and enhance the FPC efficiency. Single-glaze, low-nonselective absorbers, and double-glaze high-selective absorbers also boost the collector performance [19]. In [20], double-glazed, low-emissivity glass coatings improved the efficiency at low ambient temperatures. Low-emissivity coatings with up to 85% solar transmittance are employed in FPCs to further enhance their efficiency.

Figure 1 depicts the heat collection process using nanofluids in FPCs via a heat exchanger. One side carries the nanofluids and collects and stores energy from the collectors. In contrast, water cools the nanofluids and returns them to the tank after heat storage. The circulating pump controls the fluid flow through the collector, which is regulated by a flow control valve. Increasing the number of glass covers reduces the top heat loss and boosts efficiency by 40% at higher temperatures. To minimize heat loss, both the adsorbent plate and cover should have an emittance value of 0.1 [21]. In [22], anti-reflecting and self-cleaning coatings were introduced to enhance FPC efficiency.

Conventional solar FPCs typically employ a single glass cover with high transmittance, low iron content, and a high anti-reflective coating to minimize reflection loss. Lower-emissivity coatings are used to enhance the collector efficiency at high temperatures. Introducing an air gap between the selective absorber and cover reduces radiation losses. Double glass covers were used to further minimize the top and reduce losses. These double glass covers incorporate a low-emissivity coating between the two layers, significantly reducing reflection loss. The double glass is

Table 1. Different nanofluids and their characteristics [17, 18]

	Particle size (nm)	Volume fraction (%)	Thermal Conductivity (W/m/k)	Thermal enhancement %	Efficiency of FPC %
1. Metal					
Gold	<400	0.05-0.1	320	22	Improve efficiency by 2.3-23% overall [39]
Silver	<100	0.3-0.9	424	18	
Copper	50-100	0.1	398	41	
Aluminum	<10	0.10	273	35	
Steel	10	0.01-0.05	46	25	
2. Metal-oxide					
Alumina (Al_2O_3)	28	3-8	40	41	Efficiency improve up to 26.33% [39]
Cupric (CuO)	100	7.5	77	52	
Iron-oxide (FeO)	15	3-5	7	30	
Titanium dioxide (TiO_2)	15	0.5-5	8.37	30	
Zinc-oxide (ZnO)	10	0.1-0.5	29	25	
Silicon dioxide (SiO_2)	12	1-4	23	23	
3. Carbon					
Carbon black	190	4.4-7.7	0.182	10	Efficiency improved up to 28.6% [39]
Graphene oxide	Not specified	0-0.6	2000-5000	6.47	
Diamond/MWCNT	5-15μm	0.14-0.24	900-2320	10	
4.Working fluids					
Water	$\geq 1\mu m$	0.5-14.50	0.68	5 [70]	
Ethylene glycol	5-50microm	14.25	0.257	4.93	Efficiency improve by 5% [70]
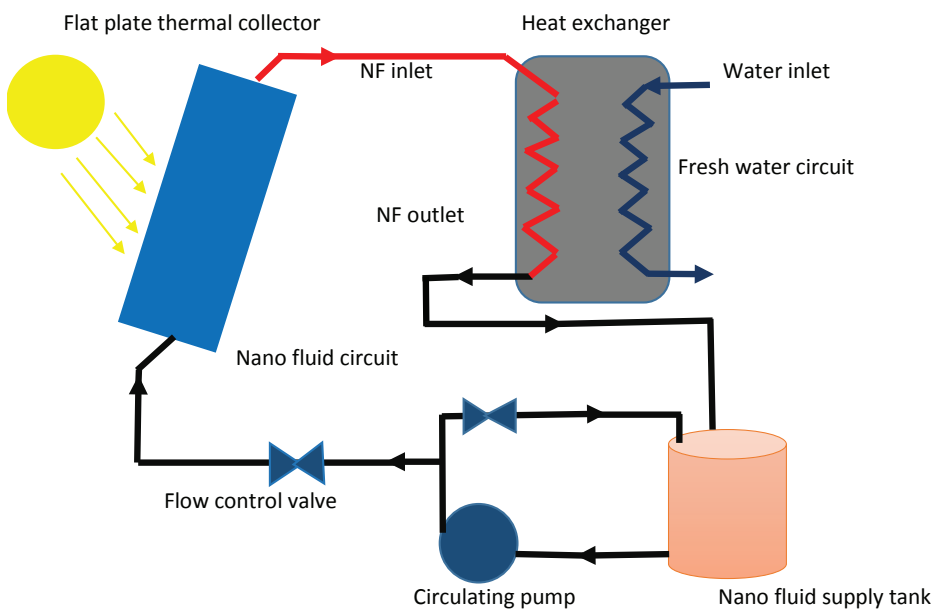
Figure 1. Flat plate heat collection process with nanofluids [From Chamsa-Ard et al. [17], with permission from MDPI].

composed of low iron content with 8 mm thickness, boasting a low emissivity coating value of 0.94 and a transmissivity of 0.5. Figure 2 illustrates a design featuring single and double glass covers.

In [23], thermal FPCs were theoretically evaluated using vacuum glazing to optimize the internal and external energy absorption configurations of the absorber. A low-emissivity coating with a value of 0.20 and a transmittance of
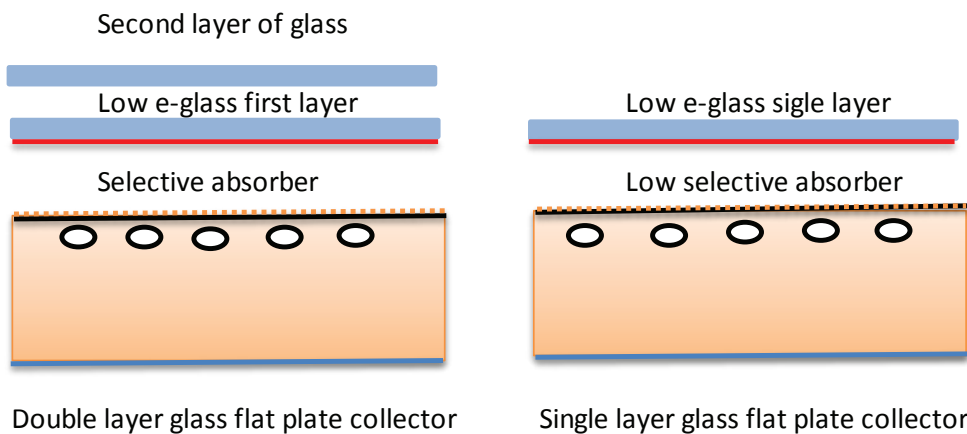
Figure 2. FPCs with double (Left) and single (Right) glass layers [From Giovannetti et al. [19], with permission from Elsevier].
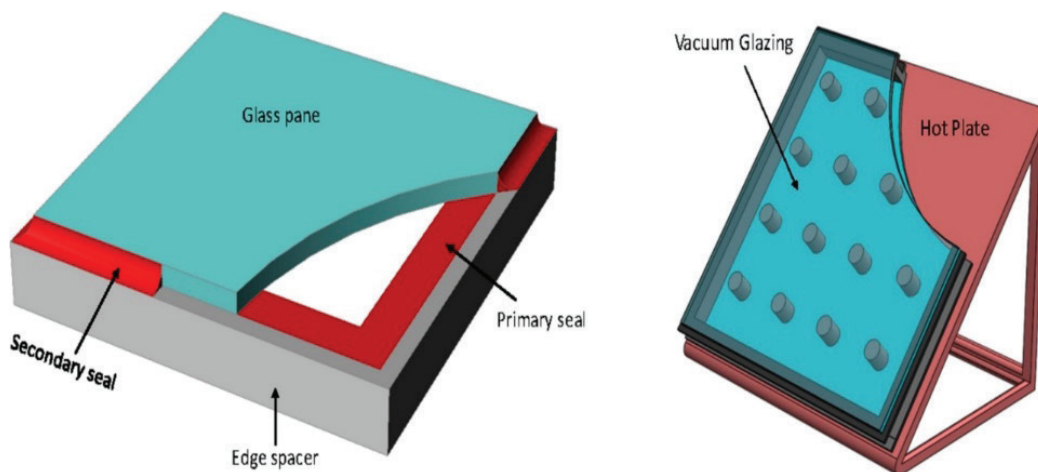

Figure 3. Vacuum glazing on FPCs with sealing details [From Arya et al. [24], with permission from Elsevier].

0.85 yielded the highest efficiency. The absorber was sealed using vacuum glazing with a glass temperature tolerance of 156°C. The vacuum glass consists of 4 mm tempered glass panes with a 0.3 mm gap. Figure 3 depicts the vacuum creation process between glass panes using edge spacers and soldering techniques, ensuring a vacuum pressure of less than 1pa and reliable sealing. Secondary seals are employed to maintain the vacuum pressure and prevent leaks due to the high melting temperature of tin alloys.

Heat loss significantly affects the thermal heat collector efficiency owing to inadequate solar radiation capture and heat transfer losses. Vacuum glass reduces the heat loss from 5.51 W/K. m2 to 3.34W/K.m2, achieving an efficiency of 58.6% with a loss coefficient of 1.68 W/K. m2 [25]. In [26], seven materials with varying concentration ratios were used to create high-transmittance vacuum glass, each measuring 300mm × 300mm × 4mm and operating at 50°C.

A study used alumina/water-based nanofluids to improve a FPC's performance, evaluating efficiency at mass flow rates of 0.1 to 0.4 kg/s. Nusselt numbers were used to determine the coefficient of performance, with additional tests using copper oxide, titanium oxide, and silicon oxide nanofluids. Despite efforts to increase efficiency by raising nanoparticle concentration by 3% and flow rate to 0.2 kg/min, there was no significant improvement due to low thermal conductivity [42]. Nanofluids notably boosted the FPC's thermal performance, improving it by 5% to 35% and extending its lifespan. They also enhanced the collector's thermal stability and conductivity. However, high viscosity, friction, and pressure drop values, compounded by low thermal stability, compromised the collector's efficiency [43]. Graphene and crystal nano-cellulose nanofluids, at 0.5% and 0.3% volumetric fractions, were used to improve collector thermal performance. However, high optical loss and volume concentration, notably at 15.81%, greatly affected collector efficiency [44]. Zinc-oxide/water and copper-oxide/water nanofluids were used to enhance the FPC's efficiency, resulting in a notable 81.64% increase.

However, their heat-bearing capacity is insufficiently low [45]. Multi-wall carbon nanotubes and alumina nanofluids were used to enhance thermal performance, resulting in a notable 26% improvement. However, they are tailored for specific conditions rather than being suitable for all weather conditions [46].

Applying magnesium oxide water-based nanofluid in FPCs showed a maximum relative error of 5.36% and a minimum of 0.20%. A concentration of 0.75% magnesium oxide water enhanced collector efficiency, but the high mean relative error significantly affected result accuracy [47]. Using GAMWCNT-water-based nanofluid effectively improved collector efficiency. Testing different concentrations led to an impressive 30.88% overall energy efficiency boost. However, the combination of nanofluids raised the inlet temperature, impacting the working fluid's performance [48]. MWCNT-water-based nanofluids were used in FPCs to improve thermal efficiency by 52.4% and exergy efficiency by 2.56%. However, the high friction factor and elevated Nusselt number values shorten the fluid's lifespan [49]. Carbon-based (MWCNT/water) and metal-based (alumina/water at 1% volume fraction) nanofluids were used to boost collector thermal performance. However, combining these nanofluids reduces the Nusselt number, affecting fluid concentration [50]. Titanium dioxide and CF-MWCNTs nanofluids improved collector efficiency by 26%, yet their temperature bearing capacity is low [51].

Clove-treated carbon nanotubes and titanium dioxide composite materials (60% to 40%) boosted FPC performance by 20.6%, along with a 22.9% increase in exergy rate. However, they have a low temperature-bearing capacity, worsened by a high pressure drop from increased flow rates [52]. A ZrO2-SiC and distilled water hybrid nanofluid boosted FPC efficiency by 75.21% across different mass flow rates. However, increasing nanofluid flow rates reduced the enhancement of the collector's exergy rate [53]. Nanofluid motion affects collector efficiency as it alters thermal conductivity, heat absorption, and heat generation [54-57]. Combining iron-oxide nanoparticles and polyethylene glycol 200 creates nanofluids for FPC fabrication. This boosts collector efficiency notably by 13.83% [58]. The CuO-MWCNT and methanol nanofluid offers high heat transfer rate, exergy efficiency, and low entropy rate. However, using a large quantity of nanofluids raises entropy, thereby reducing collector exergy efficiency [59]. In a recent study, hybrid nanofluids composed of oil and nanoparticles were used for thermal energy collection. The performance was enhanced by adding multiwall carbon nanotubes and alumina particles to the nanofluids [73]. Copper and multiwall carbon nanotube water-based nanofluids are used to enhance the thermal performance of flat plate collectors. Using this nanofluid improves the collector's efficiency by 32.25% [74]. In another study, ionanofluids and nanofluids with various base fluids, such as water, ethylene glycol, and different types of ions, were used to enhance the performance of flat plate collectors [75].

Alumina-water ethylene glycol-based nanofluid is used to enhance the thermal performance of flat plate collectors at different concentration ratios. This results in a 54.1% improvement in the collector's efficiency [76, 77]. In one study, CuO-water-based nanofluid was used to enhance the thermal performance of flat plate collectors, resulting in a 32% improvement in efficiency [78, 79]. Alumina-water-based nanofluid is employed to boost the performance of flat plate collectors [80]. Table 2 decsribes the summary of the reviewed literature.

The objective of this research is to improve the thermal efficiency of FPCs by utilizing hybrid nanofluids and vacuum glazing principles. The utilization of hybrid nanofluids enhances the efficiency of the collector, whereas vacuum glazing serves to minimize reflection losses, thereby augmenting the rate of radiation absorption. The study focuses on developing hybrid carbon and metal-based nanofluids with superior thermal conductivity, high heat-bearing capacity, and prolonged longevity. Diamond nanoparticles are incorporated for their exceptional thermal conductivity and heat-bearing properties. The proposed nanofluids consist of alumina, diamond, and ethylene glycol-based compositions, with maximum weight proportions of 0.3%, 0.1%, and 0.3% respectively. These nanofluids are circulated at a mass flow rate of 4 L/min to capture the thermal heat generated by the FPCs. Additionally, heat loss assessment is conducted using nanofluids with varying mass fractions to comprehensively evaluate collector performance. To optimize FPC design, vacuum glazing is introduced to minimize reflection loss within the absorber. The selected glass material exhibits an emissivity of 0.21 and a transmittance of 0.87%, significantly contributing to overall efficiency enhancement. The design methodology relies on simulations carried out using the Python Anaconda Jupiter notebook.

SYSTEM DESIGN

Flat-Plate Collectors

FPCs are a type of solar thermal heat collector that gathers thermal heat by moving fluids through it. The sun's irradiation radiation is absorbed by the working fluids and used. The dark surfaces of the FPCs are heated by the sun's irradiation radiation, and this heat is captured by the fluids that flow through the pipes in the absorber portions. The FPC's top cover is made of glass, and in the proposed design, vacuum glazing is used to let in the sun's high-frequency radiation while blocking its low-frequency radiation. Additionally, it prevents cold air from passing through the glass surface and reaches the absorber portions, which lose heat. For this reason, vacuum glass enhances the FPC efficiency [40].

Several fluid formulations have been proposed to improve the efficiency of thermal heat collection from FPCs. These fluids can be metal-based, metal-oxide-based,

Table 2. Literature review summary

Ref	Nanofluid	Advantages	Disadvantages	Major findings
[42]	Alumina/water-based (copper oxide, titanium oxide, and silicon oxide)	· FPC efficiency improved by 32.1% with negligible pressure drop	· Low thermal conductivity and high concentration rate which reduce the lifespan of collector	1. Thermal efficiency increased by 29.27%. 2. Improved collector's heat transfer coefficient. 3. Minimal pressure drop.
[48]	GAMWCNT-water-based	1. Exceptionally stable. 2. Environmentally safer with covalent functionalization, reducing environmental risks.	1. Low thermal conductivity 2. High inlet temperature reduces efficiency and affects the collector	1. Collector efficiency up by 30.8%. 2. Exergy efficiency rises with higher mass flow rates 3. Low cost with payback period of 1.9 years
[49]	MWCNT/water and alumina/water	1. Thermal efficiency increases by 56% with improved heat transfer rate 2. Low entropy generation value	1. High friction reduces nanofluid lifespan. 2. Shortens collector lifespan.	1. Friction factor peaks at 13.05% with 0.3% nanofluids. 2. Thermal efficiency increases by 56.69% 3. Exergy efficiency reaches 2.59% with 0.3% nanofluids
[52]	Clove-treated carbon nanotubes and titanium dioxide composite materials	1. Environmentally friendly approach 2. Enhance energy and exergy efficiency 3. Decrease collector size	1. High pressure drop 2. Low temperature bearing	1. Thermal efficiency and exergy improve by 20.6% and 22.9%. 2. Thermal conductivity improve by 18.2% at 50°C. 3. Reduce collector size by 20.5%
[72]	Carbon nanotubes and ethylene glycol	1. Enhance collector thermal efficiency. 2. High energy gain. 3. Decrease carbon emissions	1. Low thermal stability 2. Low thermal efficiency	1. Cut carbon emissions by 39.28kg/day. 2. Improve collector efficiency. 3. High inlet-outlet temperature difference.
[81]	Graphene-based organic nanofluids	1. Improve collector thermal performance. 2. Environmental friendly.	1. Laboratory-based experimental system which does not cover real-time operation. 2. Low stability and durability.	1. Overall efficiency improves by 62%. 2. Reduces exergy loss by 49.58%.
[82]	MXene/C-dot hybrid nanofluids	1. Reduces thermal corrosion. 2. Improves photo thermal efficiency.	1. High entropy generation. 2. Low thermal conductivity.	1. Reduces corrosion by 64.5%. 2. Improves thermal efficiency to 50.5%.
[83]	Silicon-carbide with distilled water	1. Better thermal conductivity and exergy efficiency.	1. IIncreases corrosion, which reduces plate life. 2. Low thermal stability.	1. Thermal efficiency improves by 77.43% 2. Exergy improves by 37.42% 3. Thermal efficiency enhanced by 0.1% SiC/DW nanofluids.

or carbon-based. In the proposed design, carbon-based nanofluids are favoured and implemented to improve the efficiency of FPCs because they are known to have high thermal stability and low heat loss.

A FPC comprises four primary components: an absorber, heat-collection tubes, glazing, and insulating material, as illustrated in Figure 4. Absorbers absorb heat and subsequently transfer it to the working fluids, while fluid tubes collect and convert this heat for practical use, such as cooling and hot water demand for buildings. Glazing plays a crucial role in minimizing the reflection loss of solar radiation. The insulating layer, positioned at the bottom, was constructed from fibrous materials designed to curtail heat loss. These components are encased within the insulating material, safeguarding them from the weather and potential damage.

A triple-glazing vacuum layer was used in the FPCs to decrease heat loss, and nanofluids were used as the working fluid. The use of ethylene-glycol-alumina-diamond-based nanofluids, in particular, improves the overall performance of FPCs. The absorber is enclosed in these collectors by an insulating layer composed of fibre materials. The glass sections of the FPC were sealed using primary and secondary seals. To achieve a vacuum of 1 mbar inside the glass of the FPC, the primary purpose of the seal is to create a vacuum. The function of the secondary seal is to sustain this vacuum over time, thereby ensuring the continued effectiveness of the collector.

The proposed design focuses on two key elements: glazing to minimize the reflection loss and heat transfer fluids. On the glazing front, a 4 mm triple-layer vacuum glass was employed to minimize the reflection losses of solar radiation to the lowest possible level. Meanwhile, on the fluid side, nanofluids, specifically ethylene
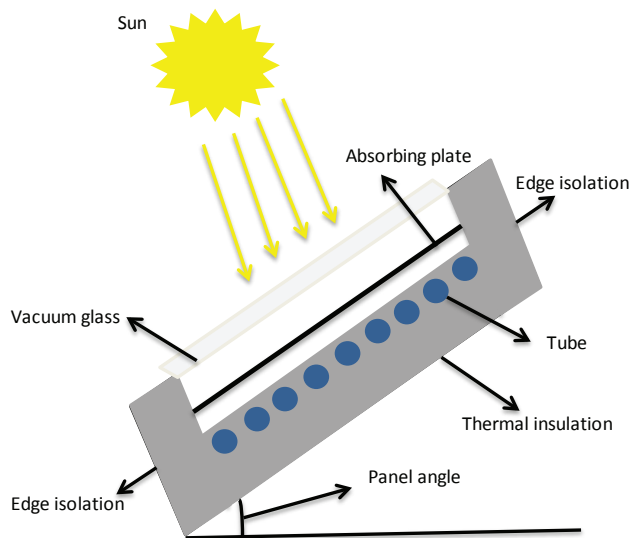
glycol-alumina-diamond-based nanofluids, are utilized to enhance the efficiency of FPCs.

Glass losses significantly affect the performance of FPCs, either by enhancing or reducing their effectiveness. These losses are primarily produced in two ways, either through reflection loss or radiation emission. The first, reflection loss, amounts to 8% [19], which is deemed relatively high, whereas the second, radiation loss, is 6% [19]. Radiation loss occurs because the absorber within the FPC absorbs solar heat, leading to heating effects in the working fluid within the channels. This heat is subsequently emitted from the top glass of the collector. On the other hand, reflection loss results from the interaction of solar light with glass, causing a reflection effect when it collides with the glass surface.
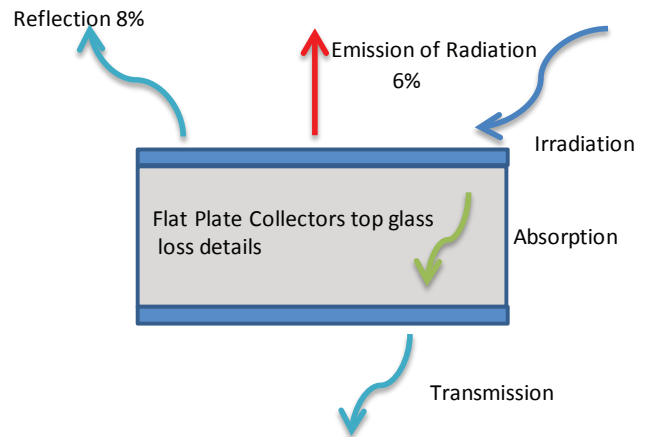

Figure 5. Heat loss details at the top glass of single glass FPCs.

Figure 4. FPCs with vacuum glass layers [From Okonkwo et al. [29], with permission from Elsevier].
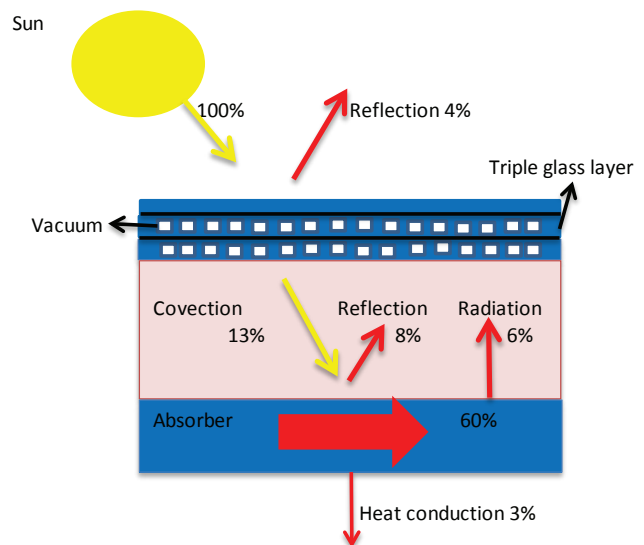

Figure 6. FPC with triple vacuum glasses.

Figure 5 shows the heat losses through the FPCs' top glass, where 8% of the solar energy was reflected off the surface of the glass. Vacuum glazing was used to reduce this reflection on the top surface of the FPC and increase the overall efficiency. The glass-related heat loss in the FPC with a triple-glaze vacuum layer is shown in Figure 6. To reduce the reflection losses caused by glass in FPCs, this specialized triple-glazing uses three layers of glass with a vacuum formed between them. Reflection loss in a typical single-glass FPC is 8%, which is considered high. However, the use of a triple-glass vacuum layer in the proposed design is expected to reduce this loss. Low-iron-content glass was chosen for this purpose owing to its advantageous properties, including a high transmittance and good emissivity of 0.90.

Vacuum Glazing

As shown in Figure 7, the vacuum glazing system consists of two sets of glass panels joined by maintaining a vacuum between them. A protective cover supported these glass panes in opposition to one another. A pressure of less than 0.1 Pa is achieved after methodically evacuating the space between these glass sets. The gas conduction and convection within the FPCs were effectively eliminated by this vacuum. Vacuum glazing improves heat transfer while minimizing the solar radiation loss from reflection. In addition, vacuum glazing uses a very thin, silver-based coating with low-iron-content glass. This coating featured a high transmissivity rate of 90% and an extremely low emissivity value of 0.03. This, in turn, reduces the solar reflection loss. Vacuum glazing has the benefit of low-air thermal insulation, which also increases energy efficiency. The amount of vacuum between the two panels lowers the solar radiation loss. The vacuum layer had a thickness of 0.4 to 0.6 mm.

Apart from having high thermal conductivity and exceptionally low carbon emission quantity, vacuum glass, which is a type of energy-saving glass, reduces carbon emissions from FPCs while also minimizing reflection and radiation emissions. A triple-layer vacuum–glass configuration is proposed in this paper. Vacuum glass is made of tempered glass with low iron content, one layer per layer. Silica-based low-iron glass with a low emissivity was used in the top layer to mitigate reflection losses. The second layer contains a 0.3-0.6 mm vacuum, and the glass extends from the panel to the insulation layer of the FPC. The vacuum within this layer is maintained at a very low level, equivalent to 1 million mbr, which minimizes conduction and further reduces the reflection of solar radiation. In the third layer, another vacuum is created, which is complemented by a low e-coating with low emissivity properties, which plays a role in reducing reflection losses. These vacuum glazing layers are designed to allow the passage of solar radiation within the 0.7-2.8μm wavelength range while effectively reducing the reflection of this radiation from the absorber plate back into the environment. The pillars provided support to the glass to ensure its stability under environmental changes. In short, triple-layer glass enhances both the emissivity rate and transmittance of solar radiation to the absorber within FPCs. The layering process is illustrated in Figure 8.
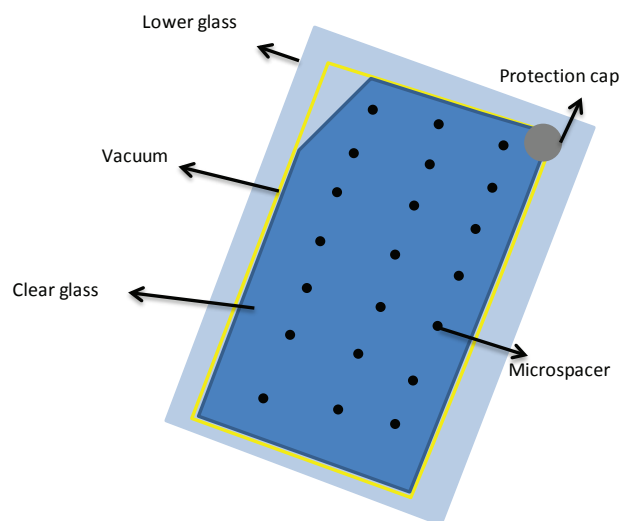

Figure 7. Vacuum glass layer of FPC [From Shemelin and Matuska [23], with permission from Wiley].
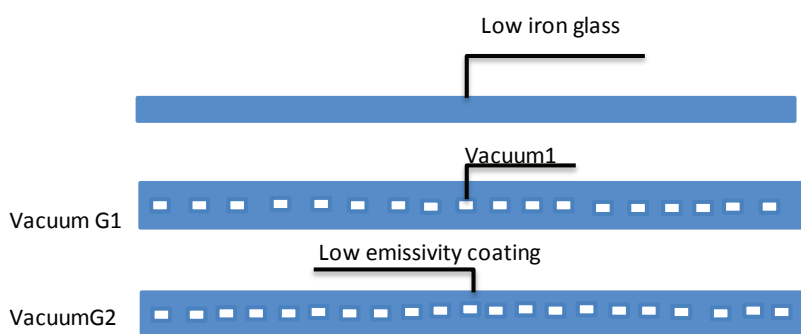

Figure 8. Details of cover glazing for FPCs [From Shemelin and Matuska [23], with permission from Wiley].

For comparison, a FPC with a single glass layer has a transmissivity rate of 0.90 and a low solar radiation emissivity rate of 0.84. Owing to the low emissivity of the glass layer, a higher heat loss is produced, which also causes an increase in radiation losses and a decrease in the overall efficiency of the FPCs. In contrast, a flat plate with a double glass layer and an anti-reflective coating was introduced to reduce the losses caused by the glass. This development improves the emissivity and transmissivity of the FPCs. The anti-reflective coating on this double layer increased the efficiency of the FPC to 78%. The double-layer glass in this configuration had an emissivity rate of 0.85 while maintaining a transmissivity of 0.90 [28].

Several critical factors are considered during the fabrication of a vacuum enclosure for a FPC. First and foremost is ensuring an adequate vacuum pressure within the enclosure, which significantly prolongs the collector's lifespan [60, 61]. Secondly, attention is given to the geometry of the enclosure, ensuring it is mechanically sound and equipped with a robust vacuum seal to envelop the absorber and establish a vacuum environment. Supporting pillars play a crucial role in maintaining the vacuum between two glass layers; these pillars must possess sufficient strength to withstand substantial pressure. To achieve a hermetic seal and maintain the vacuum, ultrasonic soldering techniques are employed. A metal alloy such as Cerasolzer 217, characterized by its high melting point of 217°C, is utilized to reinforce the vacuum. This alloy forms a resilient bond between the two glass layers, enhancing the structural integrity of the enclosure. The assembly process involves enclosing the Cerasolzer within the enclosure assembly, followed by sealing it within a secondary enclosure. Once completed, the vacuum enclosure is ready for use, effectively covering the absorber of the FPC and ensuring optimal performance [62, 63].

Ethylene Glycol-Diamond-Alumina Based Nanofluids

Nanofluids play an important role in enhancing the efficiency of thermal FPCs. To enhance the thermal heat collection, three distinct types of nanofluids were proposed in this study. These include metal oxide-based and carbon-based nanofluids, which are created using ethylene glycol, nanocrystalline diamond, and alumina. These materials are chosen based on their remarkable thermal stability when exposed to heat, resulting in minimal heat loss. This makes them ideal for the creation of nanofluids aimed at improving the efficiency of thermal heat collection in FPCs [29]. These materials also help mitigate the internal and external losses associated with the absorber plate. This further contributes to an increase in overall system efficiency.

Nanocrystalline diamond is employed to prepare nanofluids through a chemical reaction involving acids, such as sulfuric acid or nitric acid, in the presence of either distilled water or ethylene glycol. The nanodiamond content was 0.33% by weight of the nanofluids. The produced nanofluid exhibited excellent thermal stability, indicating its reaction

with acid. The operational temperature range for this type of nanofluid spans from 30°C to 80°C. The weight of each component of the nanofluid can be determined using equation (1) [29, 65, 66].

$$\emptyset_{wt}\% = (w_p/w_p + w_{bf}) \times 100 \qquad (1)$$

where $\emptyset_{wt}\%$ is the volumetric concentration, w_p is the weight fraction of the nanofluid, and w_{bf} represents the base fluid used to prepare the nanofluid.

Alumina-based nanofluids were formulated in the presence of a mixture of distilled water and ethylene glycol, with alumina containing 0.05% weight percentage. Equation (1) can also be applied to calculate the exact weight of alumina. The operational temperature range for this alumina-based nanofluid ranged from 30°C up to 80°C, and it demonstrated decent heat-bearing properties.

The weight percentage of ethylene glycol was equal to 0.1% of the weight of distilled water, which was used to prepare ethylene glycol-based nanofluids. These nanofluids also have an excellent heat-bearing capacity. To prepare the combined hybrid nanofluids from these different nanofluids, equation (2) can be used to determine the weight ratios of the different materials. Hybrid nanofluids are expected to improve the thermal efficiency of FPCs with reduced heat losses.

$$\emptyset_{wt}\% = (w_{(ND)} + w_{(alumina)} + w_{(Ethylene-glycol)})/ \\ (w_{ND} + w_{(alumina)} + w_{bf}) \times 100 \qquad (2)$$

All these materials were mixed together in the presence of base fluids (water and ethylene glycol) at a temperature of 25°C. They were stirred for 30 min and left to settle for 3-4 hours. This resting period ensures thorough mixing of the nanofluids, making them ready for heat collection in the thermal collectors.

Modeling of the nanofluids

To effectively capture heat from the flow passage, the characteristics of nanofluids used in FPCs must be well understood. In the design process, the viscosity, thermal conductivity, and specific heat capacity of nanofluids containing alumina and diamond particles were assessed. These design considerations consider variables such as temperature, solar radiation intensity, and particle volume fraction. Water and ethylene glycol were used as the base fluids in this design.

The equations for working fluids flow and heat transfer of the nanofluids is governing by using momentum law and first law of thermodynamics energy equations. [64, 66]. Equation (3) is used to determine the velocity and density of the nanodluids where ρ is the density of the nanofluids and μ_i is the velocity of the nanofluids.

$$\frac{\partial}{\partial x_i} = (\rho \mu_i) = 0 \qquad (3)$$

Equation (4) is used to determine the velocity vector of the nanofluids where p is the pressure of the fluids and $\mu_i\mu_j$ is the speed of the fluids.

$$\frac{\partial}{\partial x_j}\left(\rho\mu_i\mu_j\right) = \frac{\partial p}{\partial x_i} + \frac{\partial p}{\partial x_j}\left(v\left(\frac{\partial\mu_i}{\partial x_j} + \frac{\partial\mu_j}{\partial x_i}\right) - \mu_i\mu_j\right) \qquad (4)$$

Equation (5) represents a component of the velocity vector, pressure, and temperature of the nanofluids. Here, K denotes the thermodynamic variables, T signifies the temperature, C_p indicates the specific heat capacity of the fluids, and S_T represents the secondary temperature of the fluids.

$$\frac{\partial_p C_p \mu_j T}{\partial x_i} = \frac{\partial}{\partial x_j}\left(\frac{\kappa\partial T}{\partial x_j} - \rho C_p\mu_j T\right) + S_T \qquad (5)$$

The boundary condition at the inflow section of the nanofluid resembles laminar and uniform flow. The relation provided below illustrates this boundary condition, indicating that in laminar flow, the pressure drop value is zero.

$$u = v = 0$$

Equation (6) is used to determine the inflow in the pipe section of the nanofluids where U_{in} is the inlet heat of the fluids, T is the temperature and T_{in} is the temperature velocity of the inlet fluids.

$$w = U_{in}, T = T_{in} \qquad (6)$$

Equation (7) serves to calculate the outlet flow of the nanofluids within the collector pipe. It describes the boundary condition for this process.

$$\frac{\partial u}{\partial z} = \frac{\partial v}{\partial z} = \frac{\partial w}{\partial z}$$

$$\frac{\partial T}{\partial z} = 0 \qquad (7)$$

Equation (8) is utilized to calculate nanofluid thermal conductivity, where K_{nf} represents the effective thermal conductivity of nanofluids, K_{bf} is the thermal conductivity of base fluids, φ denotes the volume fraction, T_f is the fluid temperature, and the coefficients a_0, a_1, a_2, a_3, and a_4 are determined through regression analysis [29, 30].

$$K_{nf} = \left(a_0 + a_1 T_f + a_2 T_f^2 + a_3\varphi + a_4\varphi^2\right)K_{bf} \qquad (8)$$

The specific heat capacity of nanofluids is determined by applying equation (9), wherein C_{pnf} represents the effective thermal conductivity of the nanofluids, T_f denotes the fluid temperature, and C_{pbf} stands for the effective thermal conductivity of the base fluids.

$$C_{pnf} = \left(a_0 + a_1 T_f + a_2 T_f^2 + a_3\varphi + a_4\varphi^2\right)C_{pbf} \qquad (9)$$

Subsequently, the viscosity of the nanofluids is obtained using equation (10), where μ_{nf} represents the dynamic viscosity of the nanofluids.

$$\mu_{nf} = \left(a_0 + a_1 T_f + a_2 T_f^2 + a_3\varphi + a_4\varphi^2\right)\mu_{nf} \qquad (10)$$

The density of nanofluids can be determined using equation (11), where ρ_{bf} represents the density of the base fluids, φ_t is the thermal accommodation coefficient of the base fluids, and φ_{hnp} is the thermal accommodation coefficient of nanofluids.

$$\rho_{nf} = \rho_{bf}(1 - \varphi_t) + \varphi_{hnp}\varphi_t \qquad (11)$$

Equation (12) is utilized to calculate the internal heat transfer coefficient of FPCs, a key element in the heat transfer process where Nu represents the Nusselt number, k_f is the Darcy permeability of the fluids, and D_i is the diameter of the tube.

$$h_f = Nu. k_f/D_i \qquad (12)$$

Equation (13) is utilized for calculating the Reynolds number (Re), and equation (14) is employed to determine the Prandtl number (Pr). Both equations play a crucial role in computing the flow rates of both nanofluids and water within the flow passage of FPCs. The calculations involve parameters such as mass flow rate (m), viscosity of the fluids (μ_f), and effective thermal conductivity of the nanofluids (c_{pf}).

$$R_e = 4. m/\pi D_i\mu_f \qquad (13)$$

$$P_r = \mu_f c_{pf}/k_f \qquad (14)$$

Figure 9 illustrates the thermal conductivity characteristics of the base fluid employed in this design obtained through the utilization of equation (8). The thermal conductivity of the base fluid was measured at 25°C. The calculated values of the specific heat capacity and viscosity of the base fluid and the thermal conductivity of the base fluid were computed. The time value was taken up to 10 h, where 0 h indicates the time at 0800.

Initially, both fluids possess a thermal conductivity of 1.7 W/m·K. However, as the day progresses, there is a progressive increase in the thermal conductivity. After 6 h, it reaches a value of 1.9 W/m·K, indicating a rising trend in the thermal conductivity as the day continues.
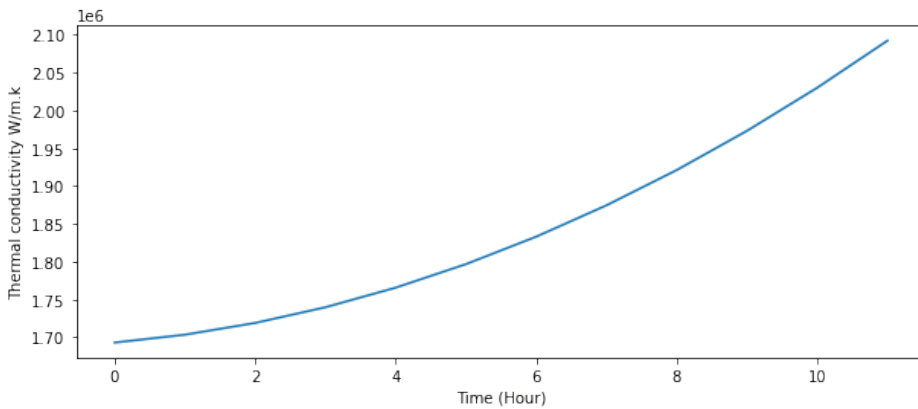
Figure 9. Thermal conductivity of base fluids with respect to time.

Figure 10 illustrates the variation in specific heat capacity at different temperature of the nanofluids simulated using equation (9). Utilizing the heat transfer equation. Initially, at a low temperature of 25°C, the specific heat capacity is 4200 J/kg.K. As temperature rises, so does the specific heat capacity of the nanofluids. At the peak temperature of 90°C, the specific heat capacity reaches its maximum at 22500 J/ kg.K. Notably, the specific heat capacity of the nanofluids is contingent upon the temperature of the fluids.

Figure 11 displays the viscosity measurements for both alumina and ethylene glycol-diamond-based nanofluids obtained through the utilization of equation (10) and (11). At a temperature of 25°C, the viscosity of alumina nanoflu- ids is recorded at 5 N.s/m², while the viscosity of ethylene glycol-diamond fluid at the same temperature stands at 21
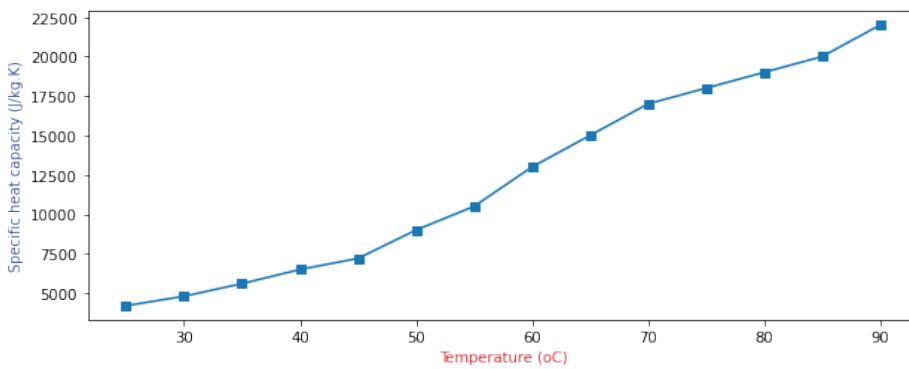

Figure 10. Specific heat capacity of the nanofluids against temperature.
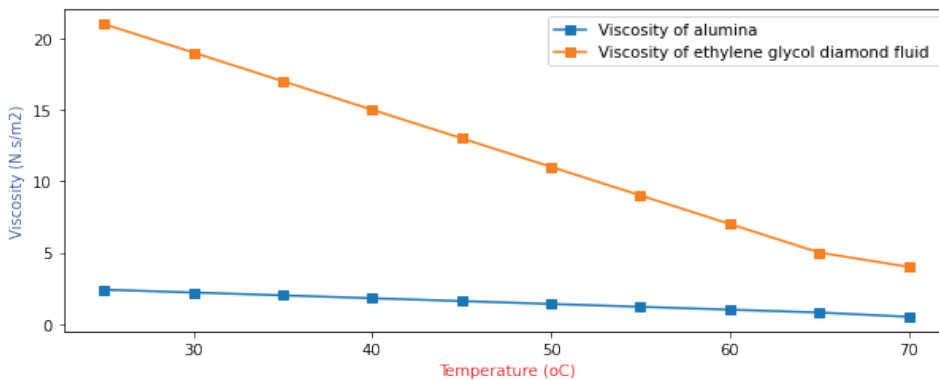

Figure 11. Viscosities of the nanofluids against temperature.

N.s/m². With increasing temperature, the viscosity of the nanofluids experiences a decrease. For instance, at a temperature of 70°C, the viscosity of alumina decreases to 0.5 N.s/m², whereas the viscosity of diamond fluids reduces to 4 N.s/m².

Modelling of Flat-Plate Collectors

Solar FPCs are situated on the rooftop of the Universiti Sains Malaysia (USM) Engineering Campus School of Electrical and Electronics Engineering (SEEE), positioned at latitude 5.1679 and longitude 100.4783. Figure 12 provides comprehensive information regarding all parameters and geometries of these solar thermal FPCs. The equations governing the behaviour of FPCs are derived from Figure 7, where β is the slope angle of the collector plane relative to the horizontal, γ represents the azimuthal angle, and θ denotes the angle of incidence of sunlight onto the FPCs.

In equation (15), δ denotes the declination angle, which signifies the angle between the Earth's axis and the surface of the cylinder relative to the Earth's orbit, and n represents the number of days in a year [31, 37].

$$\delta = 23.45 \sin\left[360\left\{284 + \frac{n}{365}\right\}\right] \quad (15)$$

Equation (16) is used to determine the solar gain of the FPCs, where the plate is placed at latitude 5.1679 and longitude 100.4783. w_1 and w_2 represent the sun angle; cosine and sine are the angles of declination and inclination of the

sun, respectively; and G_{sc} represents the standard solar constant value.

$$I_0 = 12/\pi G_{sc}(1 + \frac{0.033\cos360n}{365} * \left[\cos\varphi\cos\delta(\sin w_2 - \sin w_1) + \pi\left(w_2 - \frac{w_1}{180}\right)\sin\varphi\sin\delta\right]) \quad (16)$$

Equation (17) is used to determine the total diffused radiation of the FPC. In this equation, β denotes the tilt angle of the FPC, I_b represents the beam radiation, and R_b represents the geometric configuration of the collector with respect to its placement. In addition, $I_{\rho g}$ accounts for the surface area of the glass component of the collector.

$$I_T = I_b R_b + I_d(1 + \frac{\cos\beta}{2}) + I_{\rho g}(1 - \frac{\cos\beta}{2}) \quad (17)$$

Equation (18) is used to determine the overall heat loss at the top, bottom, and side of the FPC. U_t is the top heat loss of the FPC, U_b is the bottom heat loss of the collector, and U_e is the side loss in the collector.

$$U_L = U_t + U_b + U_e \quad (18)$$

$$U_b = (\frac{L_b}{K_b} + \frac{1}{h_{b,a}})$$

where L_b is the insulation thickness at the bottom of the plate, K_b is the thermal conductivity of the insulation, and
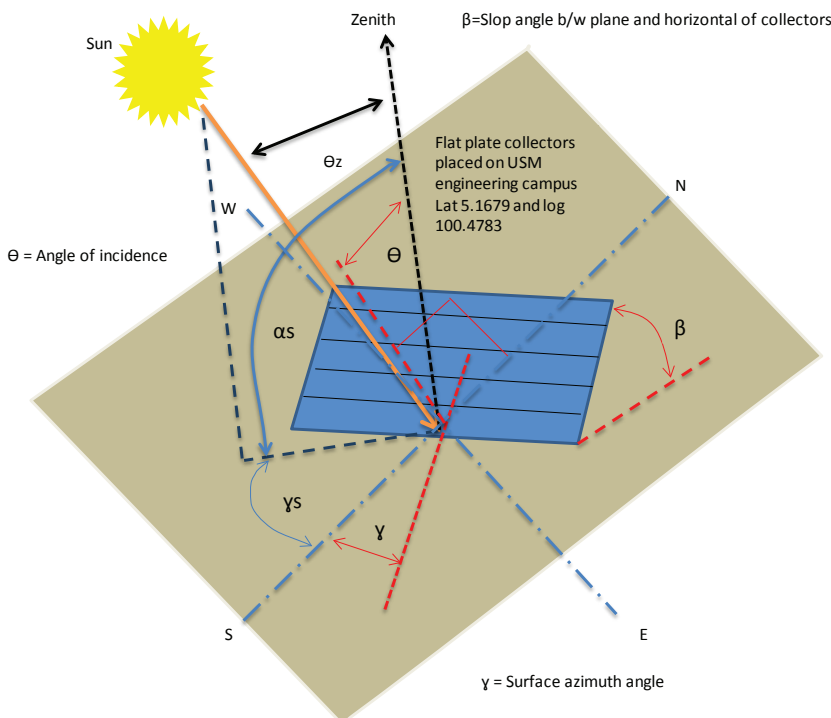

Figure 12. Solar geometry of the FPCs placed on the roof of SEEE USM.

$h_{b,a}$ is the convection heat transfer coefficient at the bottom of the FPC.

$$U_e = (\frac{L_e}{K_b} + \frac{1}{h_{e,a}})$$

where U_e is the side loss in the FPC, L_e is the side insulation thickness of the collector, K_b thermal conductivity of the insulation and $h_{e,a}$ is the heat transfer coefficient of the side of the FPC.

$$U_t = \frac{1}{R_{pc}} + \frac{1}{R_{ca}}$$

where U_t is the top heat loss of the FPC, in which R_{pc} is the thermal resistance in the absorber plate and glass cover, and R_{ca} is the thermal resistance of the glass cover and the surroundings.

$$R_{pc} = \left[h_{pc} + \frac{\sigma(T_{pm} + T_c)(T_{pm}^2 + T_c^2)}{\frac{1}{\epsilon_p} + \frac{1}{\epsilon_c} - 1}\right]^{-1}$$

where h_{pc} is the convection heat coefficient between the absorber plate and glass cover of the FPC, σ is the Boltzmann constant and T_{pm} is the mean plate temperature T_c of the glass cover. ϵ_p is the absorber plate emissivity and ϵ_c is the glass cover emissivity.

R_{ca} is the thermal resistance of the glass cover and the surroundings, in which the h_w wind heat transfer coefficient ϵ_c is the glass cover emissivity, where σ is the Boltzmann constant, T_c is the temperature of the glass cover, T_s is the sky temperature, and T_a is the ambient temperature.

$$R_{ca} = \left[h_w + \frac{\epsilon_c\sigma(T_c^4 - T_s^4)}{T_c} - T_a\right]^{-1}$$

Equation (19) is used to determine the coefficient of collector efficiency of the FPC. Where U_L is the top heat loss of the collector, W is the distance of the fluid-carrying tube from center to center, and D is the diameter of the tubes. F represents the fin efficiency of the collector, where h_{fl} is the heat-transfer coefficient of the working fluid.

$$F' = \frac{1}{U_L} / w\{1/U_l(D + (W - D)F + \frac{1}{\pi D_i h_{fl}}\} \qquad (19)$$

Equation (20) is used to determine the heat-transfer factor of the FPC where m_{cp} is the mass flow rate of the nanofluids, A is the area of the tubes, F' is the coefficient of the efficiency factor of the FPC, and U_L is the top heat loss of the collector.

$$F_r = \frac{m_{cp(nanofluid)}}{AU_L}[1 - \exp(-\frac{U_LAF'}{m_{cp(fluid)}})] \qquad (20)$$

Equation (21) is used to determine the Reynolds number value of the FPC, where m is the mass of the working fluid, D_i is the inner tube diameter, and μ_f is coefficient of the working fluids.

$$R_e = 4.m/\pi D_i\mu_f \qquad (21)$$

Equation (22) is used to determine the energy balance of the FPC, where A is the area of the collector, F_r is the heat transfer factor of the collector, S represents the total absorbed radiation of the collector, U_L is the top heat loss of the collector, T_{fl} is the temperature of the working fluid, and T_a is the ambient temperature.

$$Q = AF_r[S - U_L(T_{fl} - T_a)] \qquad (22)$$

Equation (23) is employed to determine the overall efficiency of the FPCs, where A is the surface area of the collector, Qu is the total heat loss of the FPCs, and I_T denotes the temperature value of the solar irradiated radiation intensity. This equation is useful for assessing the efficiency of FPCs utilizing carbon-based nanofluids.

$$\eta_c = Qu/I_T \times A \qquad (23)$$

Uncertainty Analysis in FPC

Minor discrepancies may exist in the collector temperature, irradiance, angle of inclination, hour angles, and total radiation absorbed by the FPC over the course of the day. These variables are manually measured to determine both the collector efficiency and the efficiency when using hybrid nanofluids. Sunrise and sunset values, utilized with a tolerance of plus or minus 5%, are subject to fractional errors. Additionally, the thermal conductivity, viscosity, and specific heat capacity values carry a fractional error of 0.75%. The glass temperature and losses within the glass of the FPCs are also subject to minor errors, each less than 1% [67, 69].

Equation (24) demonstrates that the thermal efficiency is directly proportional to both the energy collected by the collector and the total temperature absorbed by the collector..

$$\eta_c \propto \text{Energy collected by collector/}$$

$$\text{Heat on collector surface} \propto \frac{\rho V C_p(T_o - T_i)}{G_T} \qquad (24)$$

Equation (25) is employed to establish the relationship of efficiency, where ρ represents the fluid density, V denotes velocity, C_p stands for specific heat capacity, and G_T signifies the solar constant.

$$\eta_c \propto \frac{\rho V C_p (T_o - T_i)}{G_T} \propto \rho V C_p G_T^{-1} \Delta T \qquad (25)$$

Equation (26) is applied to compute the uncertainty in the efficiency of the FPC. Here, w represents the expected uncertainty value, w_ρ stands for uncertainty in fluid density, w_V signifies uncertainty in velocity, wCp denotes uncertainty in specific heat capacity value, G_T represents the solar constant, and ΔT represents the change in temperature values.

$$\frac{w \eta_c}{\eta_c} = \left[\left(\frac{w_\rho}{\rho} \right)^2 + \left(\frac{wV}{V} \right)^2 + \left(\frac{wC_p}{C_p} \right)^2 + \left(\frac{wG_T}{G_T} \right)^2 \left(\frac{w\Delta T}{\Delta T} \right)^2 \right]^{0.5} \qquad (26)$$

The projected margin of error for the collector spans from 0.75% to 1.75% when considering overall efficiency, absorbed radiation by the absorber, and heat loss.

Simulation of Flat-Plate Collectors

Figure 13 illustrates the simulation flow chart detailing the operation of the FPC incorporating nanofluids and a vacuum glass layer. Initially, the process involves determining the initial parameters of the FPC, followed by assessing its geometry and positioning. Subsequently, the total heat absorbed by the flat plate is computed, alongside the evaluation of heat losses including top, side, and bottom heat loss components. Parameters of the working fluid, such as thermal conductivity, specific heat capacity, and viscosity, are then calculated. Finally, the glass efficiency and overall efficiency of the collector are determined to comprehensively assess its performance.

The simulation of the FPC, incorporating nanofluids and vacuum glass, was conducted within the Anaconda Jupyter Notebook, utilizing the Python programming
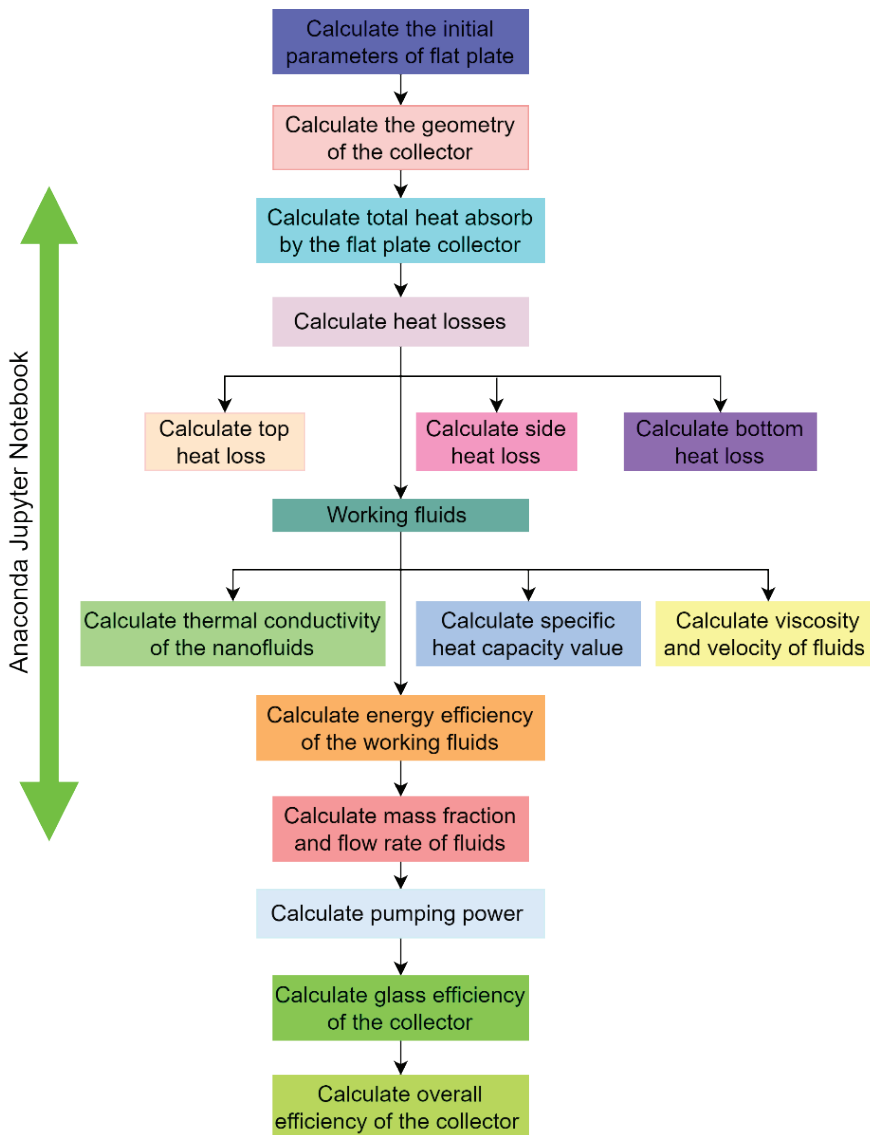

Figure 13. Simulation flow chart of the FPC with nanofluids.

Table 3. Flate plate collector specifications

FPC	Specification value used in simulation
Area (A)	4 m²
Absorbance (α)	0.96
Transmittance (τ)	0.87
Glass cover (mm)	3
Emissivity of the absorber (ε)	0.96
Emissivity of the glass cover (ε)	0.87
Insulation thickness (mm)	0.07 m²
Tilt angle (ɣs)	45⁰
Thickness of back insulation (mm)	0.08 m²
Thickness of side insulation (mm)	0.04 m²
Ambient temperature (⁰C)	25⁰C
Solar radiation intensity (W/m²)	1000W/m²

language. The simulation encompasses the set of parameters specified in Table 3, and these parameters collectively contribute to the assessment of efficiency enhancements in the FPC.

RESULTS AND DISCUSSION

In this proposed design, carbon-based nanofluids were used, in which crystalline ethylene glycol diamond and alumina were used to reduce the heat loss of the FPCs. The procedure also involved assessing the energy efficiency of the three nanofluids. This includes determining the primary heat loss in the plate heat transfer factor and the heat loss within the working fluid during energy transfer from the working fluids. In addition, the enhancement in the efficiency was calculated. The Reynolds number ranged from 800 to 2300, and the timeframe considered spanned from 8:00 to 5:00.

Figure 14 illustrates the energy efficiency of the FPC using three nanofluids: ethylene glycol, alumina, and diamond. Equation (20) is implemented for the simulation. The Reynolds number (Re) was varied from 750 to 2500, representing the nanofluid flow within the FPC. At a Re of 750, the energy efficiency of ethylene glycol was 58%; as the Re increased, the energy efficiency also increased. At a Re of 2500, the efficiency of the ethylene glycol-based nanofluids reached 68%. Similarly, for alumina-based nanofluids, the energy efficiency was 66.5% at a Re of 750, and it increased at higher Re, reaching 69% at a Re of 2500. In the case of diamond nanofluids, the energy efficiency was 67% at a Re of 750, and further increased with the Re, reaching 71.8% at a Re of 2500 in the diamond-based nanofluid case. Diamond-based nanofluids exhibit superior energy efficiency due to their exceptional thermal stability and impressive thermal conductivity, surpassing that of the other types of nanofluids.

Figure 15 shows the absorber plate temperature of the FPC corresponding to different Re values for various working nanofluids. At a Re of 750, the temperature of the ethylene-glycol-based working fluid was 40°C. As the Re increases, the temperature decreases, reaching 28°C at a Re of 2300. Increasing the flow rate of the nanofluid resulted in a lower temperature of the nanofluid extracted from the FPC.

For the alumina-based working fluid, at a Re of 750, the temperature was 37°C, and with an increase in flow rate, the temperature decreased. At a Re of 2300, the temperature of alumina-based nanofluid is 30°C. For the diamond-based nanofluid, at a Re of 750, the temperature was 36°C, and as the Re increased, the temperature decreased. At a Re of 2300, the temperature of the working fluid is 29°C. The hybrid nanofluids exhibit robust temperature-bearing capabilities owing to their high thermal conductivity. However, the temperature in the collector absorber area is influenced by fluid flow dynamics; higher flow rates result in lower temperature values.
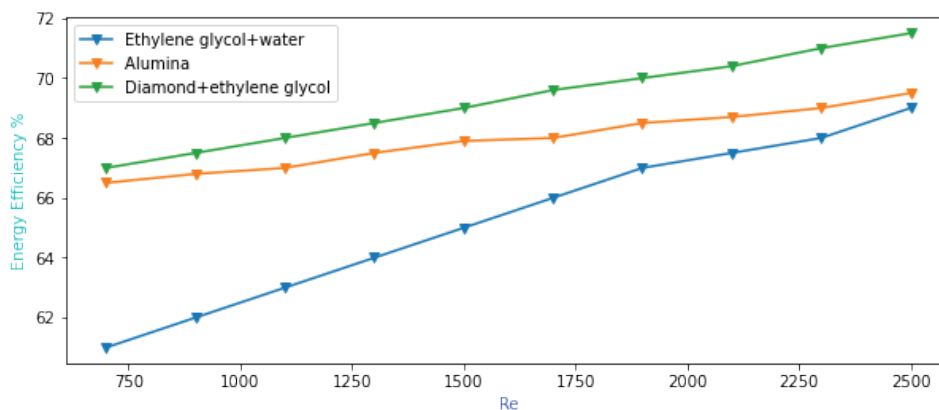
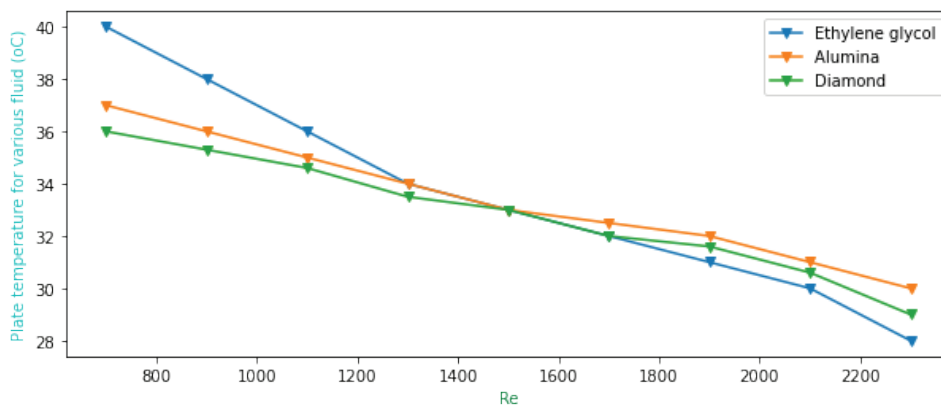**Figure 14.** Energy efficiency of all three nanofluids for the FPC.

Figure 15. Absorber plate temperature for three nanofluids with Re value.
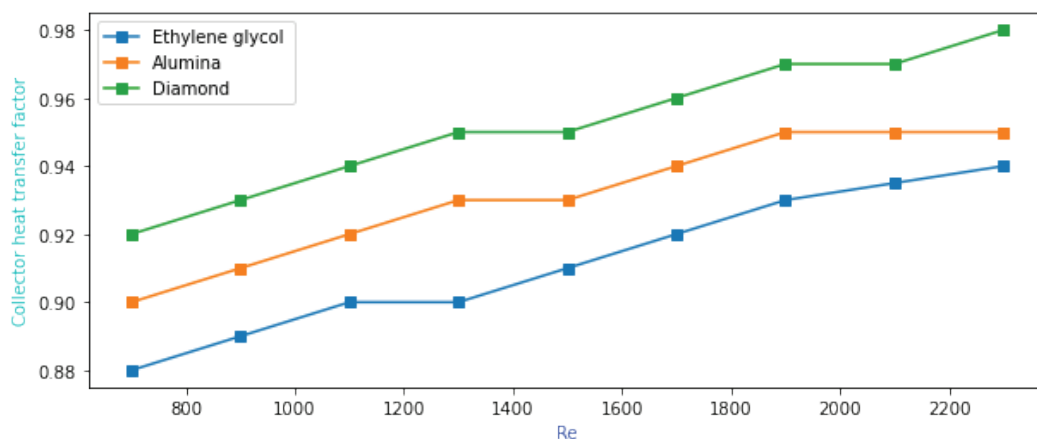

Figure 16. FPC nanofluid heat transfer factor vs. Re.

Figure 16. depicts the heat transfer factor of the FPC obtained using equation (21), illustrating that an increase in the heat transfer factor results in a decrease in the absorber temperature, leading to improved energy efficiency for both nanofluids and the FPC. At a Re of 700, the heat transfer factor of the ethylene glycol-based nanofluid was 0.88. With an increase in the Re, the heat transfer factor increased, causing a decrease in the absorber plate temperature and an enhancement in the energy efficiency of the FPC. For ethylene-glycol, at Re value of 1500, the heat transfer factor stands at 0.91, gradually rising with increasing Re values. At a Re of 2300, the heat transfer factor for the ethylene glycol-based nanofluids reached 0.93.

For the alumina-based nanofluids, the heat transfer factor at a Re of 700 was 0.90. As the Re increased, the heat transfer factor also increased, resulting in an improved energy efficiency of the FPC. At Re value of 1500, the heat transfer factor value is 0.93, and increases as the Re value rises. At a Re of 2300, the heat transfer factor peaked at 0.95, representing the maximum efficiency of the alumina-based nanofluids. In the case of the diamond-based nanofluid,

the heat transfer factor was 0.92 at a Re of 700. With an increase in the Re from 700 to 2300, the heat transfer factor increases from 0.92 to 0.98, which represents the maximum value of nanofluid heat transfer for the FPC. When the heat transfer factor was at its maximum, the efficiency of the FPC was also at its peak.

Figure 17 illustrates the top heat losses of the three nanofluids in the FPCs obtained using equation (18). Increasing the Re resulted in a decrease in the total heat loss for all nanofluids. Specifically, for ethylene glycol-based nanofluids, the maximum heat loss was 4 W/m. K at 800 Re, and as the Reynolds number increased from 800 to 2300, the top heat loss decreased from 4 to 2.6 W/m. K. As the flow rate increases, the heat loss diminishes because both radiative and convective heat loss values decrease with higher flow rates.

Similarly, for alumina-based nanofluids, the maximum heat loss is 3.8 W/m. K at 800 Re, and with an increase in the Re up to 2300, the top heat loss decreases to 2.8 W/m. K. For the diamond-based nanofluid, the top heat loss was 3.7 W/m. K at 800 Re, and as the Re increases to 2300, the top
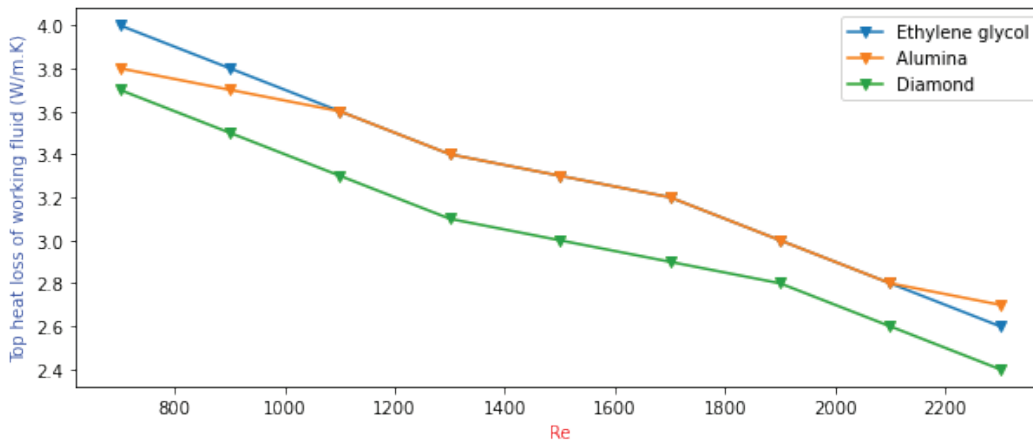
Figure 17. Top heat loss for three different nanofluids vs. Re value.

heat loss for the diamond-based nanofluid reduces to 2.4 W/m. K. Notably, the top heat loss of the working fluid was minimal for the diamond-based nanofluid, contributing to the increased efficiency of the FPC. The top heat loss in diamond-based nanofluids is minimal, attributed to their excellent thermal stability and high thermal conductivity values.

Figure 18 shows the mass fraction rate of nanofluids relative to the fluid temperature. As the temperature rises, the heat transfer properties of the nanofluid exhibit an increase corresponding to the elevated mass fraction values, thereby enhancing the efficiency of the FPC. Specifically, at 28°C, the mass fraction of the ethylene glycol-based nanofluid is 1%. With an increase in temperature and irradiated radiation intensity, the mass fraction also rises. At 40°C, the mass fraction of the ethylene glycol-based nanofluid peaks at 3.8%. For the alumina-based nanofluid, the mass fraction is 1.3% at 28°C, and it increases with the temperature, reaching 4.2% at 40°C. Notably, the diamond-based nanofluid

exhibits the highest mass fraction among all fluids, starting at 1.5% at 28°C. As the temperature climbs, the mass fraction increases, and at 40°C, it reaches its maximum value of 4.5%. This elevated mass fraction corresponds to maximum heat transfer into the fluid, thereby achieving the highest efficiency for the FPC.

In Figure 19, the FPC's environmental parameters and temperature variations are illustrated in relation to the sun's irradiated radiation. Equation (15) and (16) are implemented for the simulation. At 8:00 am, the ambient temperature is 27°C, with a sun irradiation intensity of 200W/m². As the day progresses, the ambient temperature rises, reaching a peak of 34°C around 1-2 pm, accompanied by the maximum radiation intensity of 1000W/m² during those hours.

The initial temperature of the input heat transfer fluid for the FPC at 8:00 am was 26°C. As the day advances, the input temperature increases, reaching a maximum of 33°C at 1-2 pm. Simultaneously, the output temperature of the
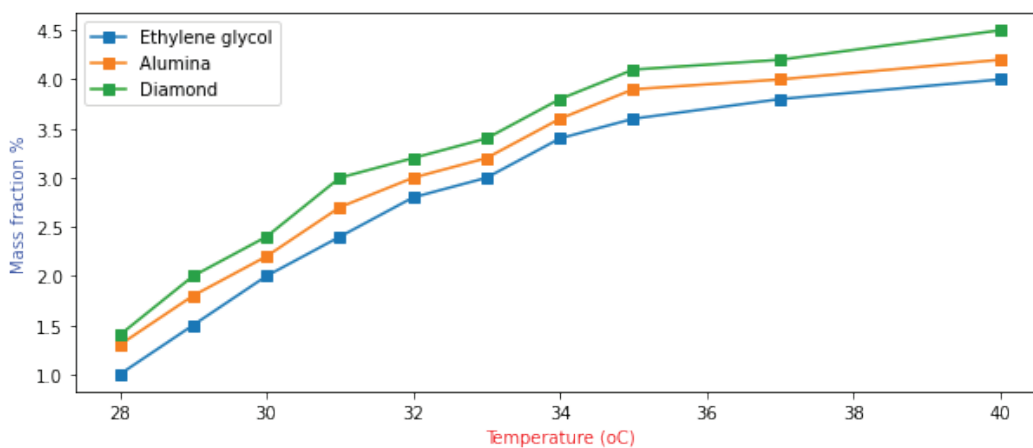

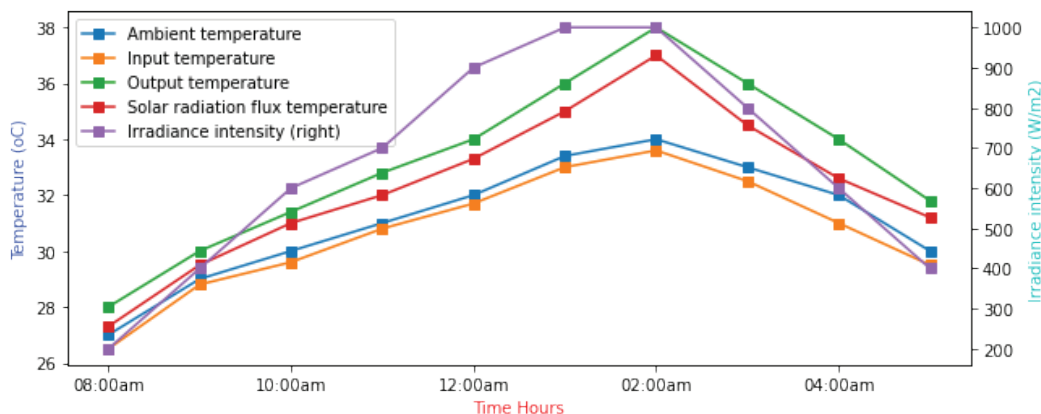**Figure 18.** Mass fraction of nanofluids with concerning to temperature.

Figure 19. Parameters of the FPC with radiation intensity value.

heat transfer fluid began at 28°C at 8:00 am and increased throughout the day, reaching 38°C during the peak hours. The solar radiation flux temperature, indicating the temperature corresponding to the irradiated radiation intensity of the sun, starts at 27°C in the morning and peaks at 36.5°C during the day's peak hours. This temperature value provides an insight into the temperature associated with the sun's radiation intensity.

In Figure 20, the mass flow rate of the nanofluids is presented alongside the corresponding efficiency for the FPCs simulated using equation (13) and (14). As the mass flow rate increased, a concurrent increase in the efficiency of the FPC was observed. For the ethylene glycol-based nanofluid, starting with a mass flow rate of 1.5 L/min, the efficiency was 30%. As the day progressed and the mass flow rate increased, efficiency also increased. At a flow rate of 4 L/min, the efficiency peaked at 68%. Similarly, for the alumina-based nanofluid, the efficiency begins at 40% with a mass flow rate of 1.5 L/min, and reaches a maximum of 74% at a mass flow rate of 4 L/min.

The diamond-based nanofluid exhibited the highest efficiency among all working fluids. At an initial mass flow rate of 1.5 L/min, the efficiency was 45%, and it reached a maximum of 82% at a mass flow rate of 4 L/min. Notably, this trend indicates that as the mass flow rate approaches its maximum value, the efficiency of the fluid also reaches its highest level.

In Figure 21, the pumping power of the FPC is shown for various nanofluids at different Re following equation (7) and (8). At a Re of 700, the pumping power for ethylene glycol was 0.2 W. As the Re increased, reflecting an increase in the flow rate, the pumping power for the nanofluids also increased. At an Re value of 2300, the pumping power for ethylene glycol reached its maximum at 2 W. For the alumina-based nanofluid, the pumping power starts at 0.3 W at a Re value of 700 and increases with increasing Re value, reaching a maximum of 2.3 W at 2300.

The pumping power for the diamond-based nanofluid was notably higher owing to the weight percentage of the diamond nanofluid. At a Re value of 700, the pumping
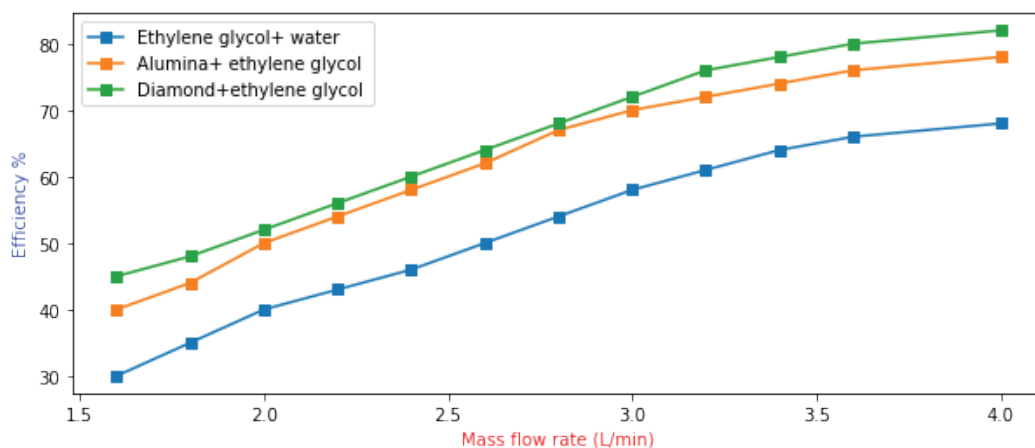

Figure 20. Mass flow rate of the nanofluids and its efficiency for FPC.
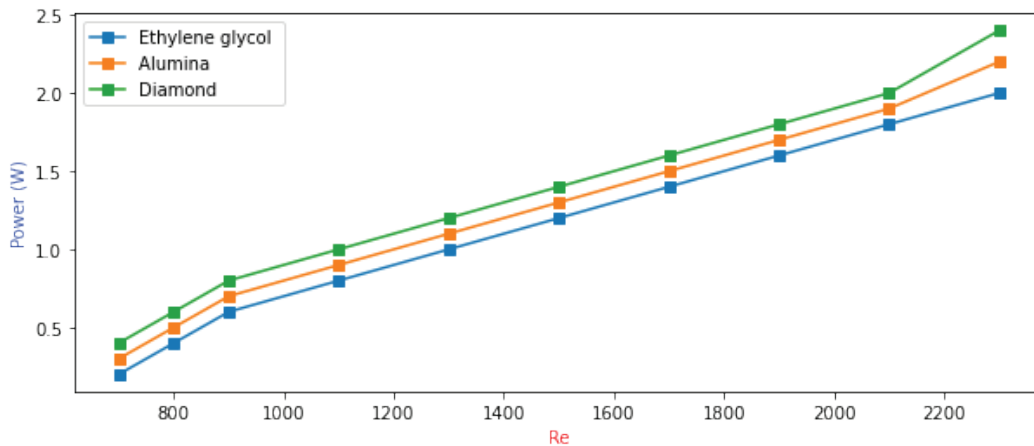
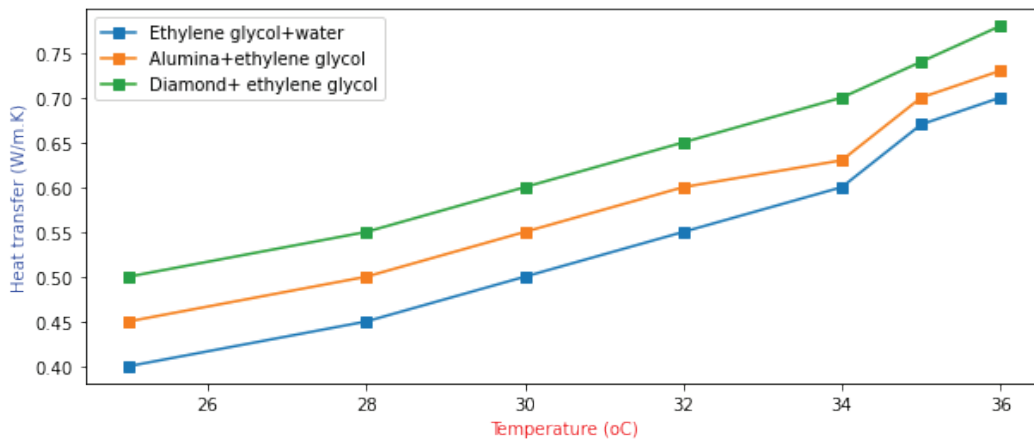**Figure 21.** Pumping power for the FPC for different nanofluids.

Figure 22. Heat transfer of different nanofluids at different temperature values of FPC.

power for the diamond-based nanofluid is 0.4 W, and at 2300 Re, the pumping power peaks at 2.5 W. This trend highlights the influence of the Re on the pumping power, with higher values corresponding to increased flow rates and, subsequently, higher pumping power.

Figure 22 shows the heat transfer characteristics of different nanofluids at various temperature values obtained through the utilization of equation (22). As the temperature increases, there is a corresponding increase in the heat transfer values for the nanofluids. For ethylene glycol-based nanofluids, the heat transfer value starts at 0.40W/m.K at 25°C. With a rise in temperature to 36°C, the heat transfer value increases from 0.40 to 0.68W/m.K. Alumina-based nanofluids exhibit a heat transfer rate of 0.45W/m.K at 25°C, which reaches its maximum at 36°C, with a value of 0.72W/m.K.

Notably, diamond-based nanofluids displayed the highest heat transfer rate among all nanofluids. At 25°C, the heat transfer rate for diamond-based nanofluid was 0.50W/m.K, and it peaked at 36°C, reaching a maximum

value of 0.78W/m.K. This trend underscores the positive correlation between temperature and heat transfer, with higher temperatures yielding higher heat transfer values for the respective nanofluids.

Figure 23 illustrates the performance of a FPC across various sun radiation intensities, comparing single, double, and triple glazing. The time span covers 08:00 am to 05:00 pm. At the outset at 08:00 am, the single glass FPC exhibits an efficiency of 25%, the double glass FPC is at 30%, and the triple glass FPC reaches 35%, all under a sun radiation intensity of 200W/m^2.

Throughout the day, the efficiency improved, reaching its zenith between 1:00 pm and 2:00 pm. During this peak period, the single glass collector achieved 72% efficiency, the double glass collector attained 76%, and the triple glass collector excelled at 82%, observed at a solar radiation intensity of 1000 W/m2. After the peak hours, the efficiency gradually declined, concluding the day with the single glass collector at 35%, the double glass collector at 40%, and the triple glass collector at 48%.
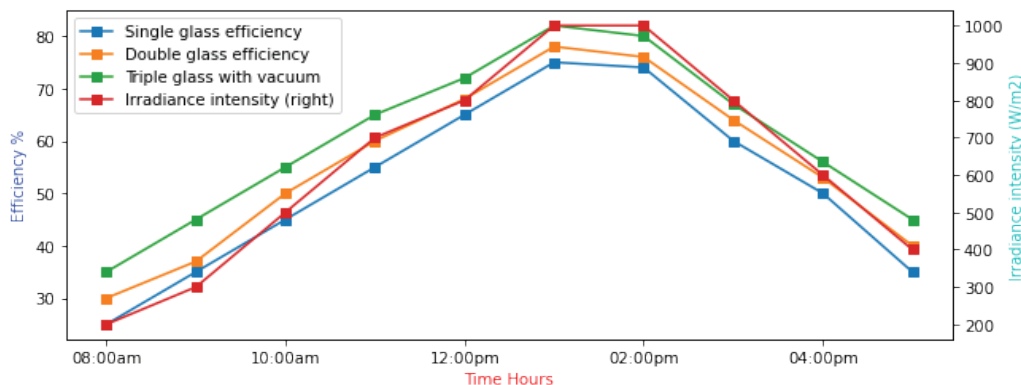
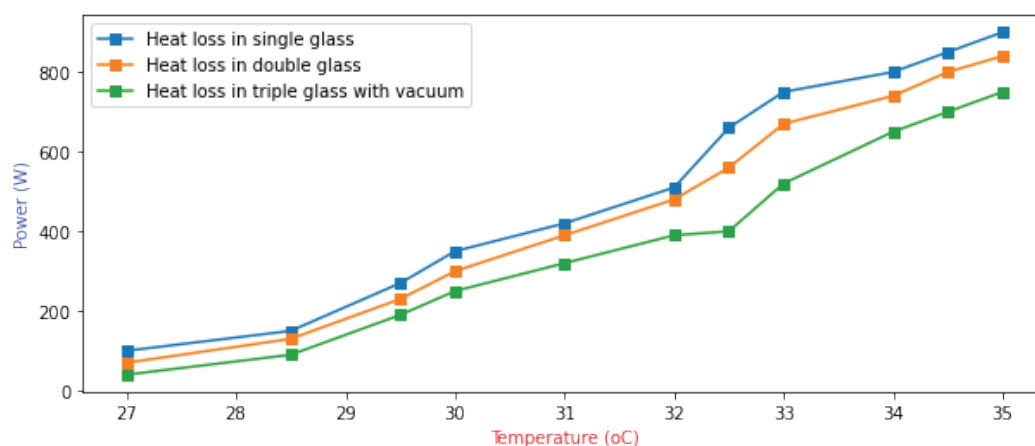**Figure 23.** Single, double and triple glass the FPC efficiency.

Figure 24. Heat loss of glass in FPC with single double and triple layer.

Figure 24 shows the heat loss in the glass layers of a FPC relative to temperature variations, considering single, double, and triple glass configurations. Initially, at a low temperature of 27°C, the power loss for a single glass layer is 70W. For a double glass FPC, it is 50W, and for a triple glass layer, it is reduced further to 30W.

As the temperature increased, the heat loss in the top glass layer also increased. At 35°C, during the peak hours of the day, the heat loss for the single glass layer rose to 850W. For the double glass configuration, it reached 780W, and for the triple glass layer, it was minimized to 700W.

Figure 25 shows the comprehensive efficiency of the FPC in relation to sun irradiance, nanofluids, and glass layers. Equation (24) is used to obtaine the result. At the beginning of the day, 08:00 am, with a sun intensity of 200W/m², the overall efficiency stands at 28%. As the day advances and sun intensity increases, the FPC's efficiency, particularly with a triple glass layer and nanofluids, experiences a notable enhancement.

During the peak hours from 1:00 pm to 2:00 pm, when the sun intensity is at its maximum, the FPC achieves a peak efficiency of 82%. However, as the sun sets, the efficiency of the FPC gradually decreases.

In Figure 26, the enhancement in the overall efficiency of the FPC is depicted, achieved through the utilization of three distinct nanofluids: ethylene glycol, alumina, and a diamond-based nanofluid, coupled with a triple glass layer incorporating a vacuum. The introduction of ethylene glycol-based nanofluids results in a 2% improvement in FPC efficiency. Alumina-based nanofluid contributes to a more substantial increase, with a 5.5% improvement. Notably, the diamond-based nanofluid demonstrates the maximum efficiency improvement at 8%. This is attributed to the diamond's exceptional heat conductivity and high thermal stability, making it particularly effective in enhancing efficiency.

Furthermore, the integration of a triple glass layer with vacuum enhances the FPC efficiency by 4%. The cumulative impact of these improvements resulted in an overall efficiency gain of 6%, elevating the efficiency of the FPC to 82%.
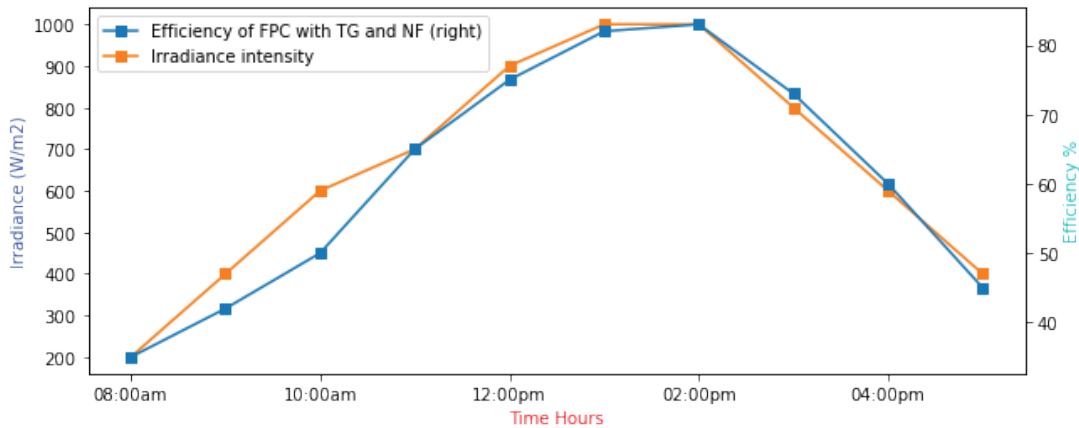
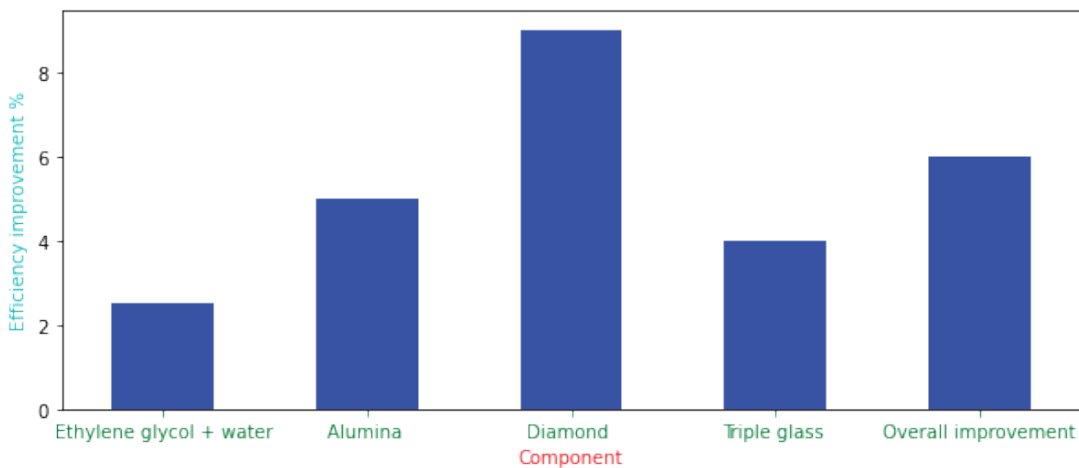**Figure 25.** Overall efficiency of FPC with triple glass and nanofluids.

Figure 26. Overall efficiency improvement of FPC with nanofluids and glazing.

Comparison of FPC Efficiency Using Ethylene-Glycol-Diamond-Alumina Nanofluids and Other Nanofluids

In [34] and [35], copper and alumina-based nanofluids were employed to enhance the efficiency of FPCs with water serving as the base solution. The research proposed the use of both hybrid and mono-nanofluids, resulting in a FPC efficiency of 78%. Table 4 provides a comprehensive overview of the physical and thermal properties of these materials, and Table 4 details the effects of nanofluids on the performance of FPCs. Alumina demonstrated good thermal stability, with a density of 3970 kg/m³ and a specific heat capacity of 765 J/kg/K. In contrast, copper possesses a higher density of 8933 kg/m³, but has a lower specific heat capacity of only 385 J/kg/K. Owing to its limited specific heat capacity, copper is considered to be less suitable as a nanofluid material for FPCs. It is worth noting that both nanofluids used in Table 4 are metal oxide-based, which may not be ideal for the long-term durability of FPCs and associated components. Additionally, the transmissivity of the glass employed may not effectively reduce the heat loss.

In the proposed design, a combination of metal oxide and carbon-based nanofluids was employed to enhance the efficiency of FPCs, as illustrated in Figure 23. In the figure, a high initial starting efficiency factor corresponds to a low collector efficiency. However, as the day progressed, the efficiency of the FPC increased, reaching a peak when the efficiency factor reached 0.18%. At this stage, the FPC achieves an impressive efficiency of 82%. Diamond exhibits a specific heat capacity of 1500 J/kg/K and a high heat-bearing capacity of 3515 kg/m³. The nanoparticles employed had a size range of 100–200 nm, and the volume fraction was distributed at 0.3:0.1:0.3. The vacuum glass used in the proposed design has a high transmissivity rate of 0.87, which helps to reduce the loss of FPCs and improve the overall performance. A comparison between the flat plate designs using different numbers of glass layers is presented in Table 5.

Table 4. Physical properties of literature nanofluid and proposed nanofluids

Nanoparticle	Δ (Kg.m^{-3})	Cp (J. Kg^{-1}. K$_{-1}$)	Particle Size (nm)	Volume fraction (%)	Glass transmissivity (%) of FPCs	Fluid type	Efficiency of FPC (%)
Al$_2$O$_3$ [34, 35]	3970	765	30	0.1	0.85	Metal-oxide	78
Cu [34, 35]	8933	385	40	0.1	0.85	Metal-oxide	
Physical propeties of the proposed nanofluids.							
Al$_2$O$_3$	3970	765	100	0.3	0.87	Metal-oxide	82
Diamond	3515	1500	200	0.1	0.87	Carbon-based	
Ethylene-glycol	1058	4186.8	Liquid	0.3	0.87	Carbon-base	

Table 5. Comparison of single, double, and triple-layer glass for FPCs

Glass layer	Glass material iron content	Solar transmittance	Emissivity	Efficiency with top glazing
Single glass [28]	Low	0.90	0.84	75
Double glass with anti-reflecting coating [28]	Low	0.90	0.85	78
Triple glass layer with vacuum.	Low	0.96	0.87	82

The proposed design introduces various nanofluids to enhance FPC efficiency and address heat transfer fluid and convective losses. One advantage lies in the improved thermal conductivity associated with better nanofluid stability, particularly evident in ethylene-glycol-diamond-alumina nanofluids. Additionally, surfactant utilization can optimize particle surface characteristics, further boosting thermal conductivity. However, the choice of nanoparticle size is critical as it directly impacts collector performance, and high viscosity in diamond-alumina nanofluids can increase pumping power, thereby reducing efficiency. This highlights a disadvantage, as elevated pumping power diminishes collector performance. Moreover, the increased cost of nanofluids and heightened corrosion rates due to their large molecular size and weight pose significant challenges, shortening the collector's lifespan.

CONCLUSION

In summary, this study has effectively enhanced the efficiency of flat-plate solar collectors through targeted optimization of working fluids, radiation intensity, and the integration of innovative materials such as carbon-based and metal-oxide-based nanofluids, alongside triple-layer vacuum glass. Utilization of low-iron-content triple-layer vacuum glass and novel ethylene-glycol-diamond-alumina-based hybrid nanofluids has led to promising outcomes in reducing heat loss. Detailed analysis reveals that ethylene-glycol fluid achieves 58% efficiency at 40°C, alumina nanofluid 68% at 38°C, and diamond-based nanofluid 71.8% at 36°C. Heat loss with all three nanofluids ranges from 4 W/m.K to 2.4 W/m.K, corresponding to efficient heat retention. Despite higher viscosity of the diamond-based nanofluid, resulting in increased

pumping power requirements, pressure drop remains low. Moreover, transitioning from single- to triple-glass configurations significantly boosts efficiency from 72% to 82%, accompanied by reduced heat loss. Overall, nanofluid utilization and triple glazing contribute to an 8% and 4% improvement in collector efficiency, respectively, culminating in an overall efficiency of 82%. This innovative design, simulated using Anaconda Jupyter Notebook and Python, underscores its potential to advance sustainable energy solutions in solar energy collection. Future research will focus on investigating the efficacy of surfactants in nanofluids to bolster their thermal stability and properties, aiming to overcome challenges like efficiency loss and particle settling, which could compromise long-term stability and thermo-physical characteristics. Moreover, conducting comprehensive cost analyses over extended nanofluid lifespans will be crucial, especially if longevity is a concern. These investigations will provide valuable insights into nanofluid behavior, facilitating the development of more efficient and sustainable applications in solar energy collection.

NOMENCLATURE

A	Area of the flat plate collectors (m^2)
W	Sunrise and sunset angle of the sun
D	Diameter of the tubes of the flat plate (m^2)
Cb	Bond Conductance (W/m.K)
F	Efficiency %
F'	Efficiency Factor (collector) %
Fr	Fractional efficiency %
h r, p-g	Radiative heat-transfer coefficient from to glass (W)
h c, p-g	Convective heat transfer coefficient from plate to glass (W)

h r, g	Radiative heat transfer coefficient ambient (W/m². K)
I	Terrestrial Solar radiation (Wh)
Io	Extra Terrestrial solar radiation
Kt	Clearness index
Knf	Thermal conductivity of nanofluid (W/m.K)
Kf	Thermal conductivity of base fluid (W/m.K)
M	mass flow rate
Q	Overall heat loss (wh)
S	Absorbed solar radiation (wh)
Ta	Ambient temperature (K)
Tg	Glass temperature (K)
Tp	Plate Temperature (K)
Tft	Fluid inlet temperature (°C)
Ul	Heat loss (wh)
N	Number of days of the year
Gsc	Solar gain (W)
Id	Diffused radiation (W)
Ib	Base fluids
Kair	Air temperature (°C)
L	Length (m)
Ut	Thickness loss in glass (W/m.k)
hc	Heat transfer for tubes (W)
hf	Heat transfer coefficient of fluids (W/m.K)
nf	Nanofluids
S	Side loss of the flat plate collectors (W)
IT	Total diffused radiation of flat plate collectors (W/m²)
Qu	Heat flux (W)
ρg	Density of glass
εp	Transmissivity of plate
εg	Transmissivity of the glass
Wp	Weight fraction of nanofluids
Wbp	Weight fraction of base fluid
Knf	Thermal conductivity of nanofluids W/m. k
Knb	Thermal conductivity of base fluid W/m. k
Tf	Temperature of fluids (°C)
ρbf	Density of base fluids
ρnf	Density of nanofluids
μf	Viscosity of fluids
Nu	Nusselt number
hnp	Hybrid nanofluids
Re	Reynolds number

Greek symbols

δ	Declination
θ	Incident angle (degree)
β	Coefficient of volumetric expansion (K-1)
τ	Transmittance
α	Absorbance
$\emptyset$	Volume Fraction (%)
γ	Azimuthal angle

ACKNOWLEDGMENT

AUTHORSHIP CONTRIBUTIONS

Authors equally contributed to this work.

DATA AVAILABILITY STATEMENT

The authors confirm that the data that supports the findings of this study are available within the article. Raw data that support the finding of this study are available from the corresponding author, upon reasonable request.

CONFLICT OF INTEREST

The authors declared no potential conflicts of interest with respect to the research, authorship, and/or publication of this article.

ETHICS

There are no ethical issues with the publication of this manuscript.

REFERENCES

[1] Alshuhail LA, Shaik F, Sundar LS. Thermal efficiency enhancement of mono and hybrid nanofluids in solar thermal applications–A review. Alex Eng J 2023;68:365–404. [CrossRef]

[2] Vărdaru A, Huminic G, Huminic A, Fleacă C, Dumitrache F, Morjan I. Synthesis, characterization and thermal conductivity of water-based graphene oxide–silicon hybrid nanofluids: An experimental approach. Alex Eng J 2022;61:12111–12122. [CrossRef]

[3] Nabi H, Pourfallah M, Gholinia M, Jahanian O. Increasing heat transfer in flat plate solar collectors using various forms of turbulence-inducing elements and CNTs-CuO hybrid nanofluids. Case Stud Therm Eng 2022;33:101909. [CrossRef]

[4] Eltaweel M, Abdel-Rehim AA. Energy and exergy analysis of a thermosiphon and forced-circulation flat-plate solar collector using MWCNT/water nanofluid. Case Stud Therm Eng 2019;14:100416. [CrossRef]

[5] Mirzaei M, Hosseini SMS, Kashkooli AMM. Assessment of Al_2O_3 nanoparticles for the optimal operation of the flat plate solar collector. Appl Therm Eng 2018;134:68–77. [CrossRef]

[6] Ashour AF, El-Awady AT, Tawfik MA. Numerical investigation on the thermal performance of a flat plate solar collector using ZnO & CuO water nanofluids under Egyptian weathering conditions. Energy 2022;240:122743. [CrossRef]

[7] Stalin PMJ, Arjunan TV, Almeshaal M, Murugesan P, Prabu B, Kumar PM. Utilization of zinc-ferrite/water hybrid nanofluids on thermal performance of a flat plate solar collector—a thermal modeling approach. Environ Sci Pollut Res Int 2022;29:78848–78861. [CrossRef]

[8] Sharafeldin MA, Gróf G. Experimental investigation of flat plate solar collector using CeO_2-water nanofluid. Energy Convers Manag 2018;155:32–41. [CrossRef]

[9] Farajzadeh E, Movahed S, Hosseini R. Experimental and numerical investigations on the effect of Al_2O_3/TiO_2H_2O nanofluids on thermal efficiency of the flat plate solar collector. Renew Energy 2018;118:122–130. [CrossRef]

[10] Moravej M, Bozorg MV, Guan Y, Li LKB, Doranehgard MH, Hong K, et al. Enhancing the efficiency of a symmetric flat-plate solar collector via the use of rutile TiO_2-water nanofluids. Sustain Energy Technol Assess 2020;40:100783. [CrossRef]

[11] Farhana K, Kadirgama K, Mohammed HA, Ramasamy D, Samykano M, Saidur R. Analysis of efficiency enhancement of flat plate solar collector using crystal nano-cellulose (CNC) nanofluids. Sustain Energy Technol Assess 2021;45:101049. [CrossRef]

[12] Ranga Babu JA. Thermodynamic analysis of hybrid nanofluid based solar flat plate collector. World J Eng 2018;15:27–39. [CrossRef]

[13] Mostafizur RM, Rasul MG, Nabi MN. Energy and exergy analyses of a flat plate solar collector using various nanofluids: An analytical approach. Energies 2021;14:4305. [CrossRef]

[14] Kumar LH, Kazi SN, Masjuki HH, Zubir MNM, Jahan A, Bhinitha CJA. Energy, exergy and economic analysis of liquid flat-plate solar collector using green covalent functionalized graphene nanoplatelets. Appl Therm Eng 2021;192:116916. [CrossRef]

[15] Mahamude ASF, Harun WSW, Kadirgama K, Ramasamy D, Farhana K, Saleh K, et al. Experimental study on the efficiency improvement of flat plate solar collectors using hybrid nanofluids graphene/waste cotton. Energies 2022;15:2309. [CrossRef]

[16] Alawi OA, Mohamed Kamar H, Abdelrazek AH, Mallah AR, Mohammed HA, Abdulla AI, et al. Hydrothermal and energy analysis of flat plate solar collector using copper oxide nanomaterials with different morphologies: Economic performance. Sustain Energy Technol Assess 2022;49:101772. [CrossRef]

[17] Chamsa-Ard W, Brundavanam S, Fung CC, Fawcett D, Poinern G. Nanofluid types, their synthesis, properties and incorporation in direct solar thermal collectors: A review. Nanomaterials (Basel) 2017;7:131. [CrossRef]

[18] Alawi OA, Mohamed Kamar H, Mallah AR, Mohammed HA, Kazi SN, Che Sidik NA, et al. Nanofluids for flat plate solar collectors: Fundamentals and applications. J Clean Prod 2021;291:125725. [CrossRef]

[19] Giovannetti F, Föste S, Ehrmann N, Rockendorf G. High transmittance, low emissivity glass covers for flat plate collectors: Applications and performance. Sol Energy 2014;104:52–59. [CrossRef]

[20] Ehrmann N, Reineke-Koch R. Selectively coated high efficiency glazing for solar-thermal flat-plate collectors. Thin Solid Films 2012;520:4214–4218. [CrossRef]

[21] Pourfayaz F, Shirmohammadi R, Maleki A, Kasaeian A. Improvement of solar flat-plate collector performance by optimum tilt angle and minimizing top heat loss coefficient using particle swarm optimization. Energy Sci Eng 2020;8:2771–2783. [CrossRef]

[22] Ajeena AM, Víg P, Farkas I. Anti-reflection and self-cleaning nanocoating to improve the performance of flat plate solar collector. Eur J Energy Res 2022;2:13–18. [CrossRef]

[23] Shemelin V, Matuska T. Detailed modeling of flat plate solar collector with vacuum glazing. Int J Photoenergy 2017:1587592. [CrossRef]

[24] Arya F, Hyde T, Henshall P, Eames P, Moss R, Shire S, et al. Fabrication analysis of flat vacuum enclosures for solar collectors sealed with Cerasolzer 217. Sol Energy 2021;220:635–649. [CrossRef]

[25] Messaouda A, Hamdi M, Hazami M, Guizani AA. Analysis of an integrated collector storage system with vacuum glazing and compound parabolic concentrator. Appl Therm Eng 2020;169:114958. [CrossRef]

[26] Memon S, Fang Y, Eames PC. The influence of low-temperature surface induction on evacuation, pump-out hole sealing and thermal performance of composite edge-sealed vacuum insulated glazing. Renew Energy 2019;135:450–464. [CrossRef]

[27] Sun C, Liu Y, Duan C, Zheng Y, Chang H, Shu S. A mathematical model to investigate on the thermal performance of a flat plate solar air collector and its experimental verification. Energy Convers Manag 2016;115:43–51. [CrossRef]

[28] Rashid KF, Hamakhan IA, Mohammed CH. Dynamic simulation and optimization of flat plate solar collector parameters using the MATLAB program for Erbil-Iraq climate condition. Al-Rafidain Eng J 2022;27:127–139. [CrossRef]

[29] Okonkwo EC, Wole-Osho I, Kavaz D, Abid M, Al-Ansari T. Thermodynamic evaluation and optimization of a flat plate collector operating with alumina and iron mono and hybrid nanofluids. Sustain Energy Technol Assess 2020;37:100636. [CrossRef]

[30] Delavari V, Hashemabadi SH. CFD simulation of heat transfer enhancement of Al2O3/water and Al2O3/ethylene glycol nanofluids in a car radiator. Appl Therm Eng 2014;73:380–390. [CrossRef]

[31] Baccoli R, Mastino CC, Innamorati R, Serra L, Curreli S, Ghiani E, et al. A mathematical model of a solar collector augmented by a flat plate above reflector: Optimum inclination of collector and reflector. Energy Procedia 2015;81:205–214. [CrossRef]

[32] Mahanta DK. Mathematical modeling of flat plate solar collector. Proceedings of 2020 IEEE International Conference on Power Electronics, Drives and Energy Systems (PEDES), Jaipur, India, 16-19 December 2020. pp. 1–5. [CrossRef]

[33] Merembayev T, Amirgaliyev Y, Kunelbayev M, Yedilkhan D. Thermal loss analysis of a flat plate solar collector using numerical simulation. Comput Mater Contin 2022;73:4627–4640. [CrossRef]

[34] Bamisile O, Cai D, Adun H, Adedeji M, Dagbasi M, Dika F, et al. A brief review and comparative evaluation of nanofluid application in solar parabolic trough and flat plate collectors. Energy Rep 2022;8:156–166. [CrossRef]

[35] Yurddaş A, Çerçi Y, Sarı Çavdar P, Bektaş A. The effects of the use of hybrid and mono nanofluids on thermal performance in flat-plate solar collectors. Environ Prog Sustain Energy 2022;41:e13770. [CrossRef]

[36] Mustafa J, Alqaed S, Sharifpur M. Evaluation of energy efficiency, visualized energy, and production of environmental pollutants of a solar flat plate collector containing hybrid nanofluid. Sustain Energy Technol Assess 2022;53:102399. [CrossRef]

[37] Said Z, Sharma P, Sundar LS, Tran VD. Using Bayesian optimization and ensemble boosted regression trees for optimizing thermal performance of solar flat plate collector under thermosyphon condition employing MWCNT-Fe3O4/water hybrid nanofluids. Sustain Energy Technol Assess 2022;53:102708. [CrossRef]

[38] Shehram M, Javid T, Khalid Z. Hybrid multijunction PV and CST based solar cooling system using flat plate collector and graphene based nanofluid. Proceedings of 2021 6th International Electrical and Electronics Engineering Conference (IEEC 2021), April, 2021, Karachi, Pakistan.

[39] Zayed ME, Zhao J, Du Y, Kabeel AE, Shalaby SM. Factors affecting the thermal performance of the flat plate solar collector using nanofluids: A review. Sol Energy 2019;182:382–396. [CrossRef]

[40] Chen CQ, Diao YH, Zhao YH, Wang ZY, Zhu TT, Wang TY, et al. Numerical evaluation of the thermal performance of different types of double glazing flat-plate solar air collectors. Energy 2021;233:121087. [CrossRef]

[41] Ajeena AM, Víg P, Farkas I. Anti-reflection and self-cleaning nanocoating to improve the performance of flat plate solar collector. Eur J Energy Res 2022;2:13–18. [CrossRef]

[42] Desisa TR. Experimental and numerical investigation of heat transfer characteristics in solar flat plate collector using nanofluids. Int J Thermofluids 2023;18:100325. [CrossRef]

[43] García-Rincón MA, Flores-Prieto JJ. Nanofluids stability in flat-plate solar collectors: A review. Sol Energy Mater Sol Cells 2024;271:112832. [CrossRef]

[44] Mahamude ASF, Wan Harun WS, Kadirgama K, Ramasamy D, Farhana K, Saleh K, et al. Experimental study on the efficiency improvement of flat plate solar collectors using hybrid nanofluids graphene/waste cotton. Energies 2022;15:2309. [CrossRef]

[45] Ashour AF, El-Awady AT, Tawfik MA. Numerical investigation on the thermal performance of a flat plate solar collector using ZnO & CuO water nanofluids under Egyptian weathering conditions. Energy 2022;240:122743. [CrossRef]

[46] Elshazly E, Abdel-Rehim AA, El-Mahallawi I. 4E study of experimental thermal performance enhancement of flat plate solar collectors using MWCNT, Al2O3, and hybrid MWCNT/Al2O3 nanofluids. Results Eng 2022;16:100723. [CrossRef]

[47] Geovo L, Dal Ri G, Kumar R, Verma SK, Roberts JJ, Mendiburu AZ. Theoretical model for flat plate solar collectors operating with nanofluids: Case study for Porto Alegre, Brazil. Energy 2023;263:125698. [CrossRef]

[48] Amar M, Akram N, Chaudhary GQ, Kazi SN, Soudagar MEM, Mubarak NM, et al. Energy, exergy and economic (3E) analysis of flat-plate solar collector using novel environmental friendly nanofluid. Sci Rep 2023;13:411. [CrossRef]

[49] Mouli KVVC, Sundar LS, Alklaibi AM, Said Z, Sharma KV, Punnaiah V, et al. Exergy efficiency and entropy analysis of MWCNT/water nanofluid in a thermosyphon flat plate collector. Sustain Energy Technol Assess 2023;55:102911. [CrossRef]

[50] Nuhash MM, Alam MI, Zihad A, Hasan MJ, Duan F, Bhuiyan AA, et al. Enhancing energy harvesting performance of a flat plate solar collector through integrated carbon-based and metal-based nanofluids. Results Eng 2023;19:101276. [CrossRef]

[51] Hussein OA, Rajab MH, Alawi OA, Falah MW, Abdelrazek AH, Ahmed W, et al. Multiwalled carbon nanotubes-titanium dioxide nanocomposite for flat plate solar collectors applications. Appl Therm Eng 2023;229:120545. [CrossRef]

[52] Alfellag MA, Kamar HM, Abidin U, Kazi SN, Alawi OA, Muhsan AS, et al. Green synthesized clove-treated carbon nanotubes/titanium dioxide hybrid nanofluids for enhancing flat-plate solar collector performance. Appl Therm Eng 2024;122982. [CrossRef]

[53] Ajeena AM, Farkas I, Víg P. Performance enhancement of flat plate solar collector using ZrO2-SiC/DW hybrid nanofluid: A comprehensive experimental study. Energy Convers Manag 2023;20:100458. [CrossRef]

[54] Tarakaramu N, Sivakumar N, Tamam N, Satya Narayana PV, Ramalingam S. Theoretical analysis of Arrhenius activation energy on 3D MHD nanofluid flow with convective boundary condition. Mod Phys Lett B 2024;38:2341009. [CrossRef]

[55] Tarakaramu N, Reddappa B, Radha G, Abduvalieva D, Sivakumar N, Awwad FA, et al. Thermal radiation and heat generation on three-dimensional Casson fluid motion via porous stretching surface with variable thermal conductivity. Open Phys 2023;21:20230137. [CrossRef]

[56] Masthanaiah Y, Tarakaramu N, Khan MI, Rushikesava A, Ben Moussa S, Fadhl BM, et al. Impact of viscous dissipation and entropy generation on cold liquid via channel with porous medium by analytical analysis. Case Stud Therm Eng 2023;47:103059. [CrossRef]

[57] Jagadeesh S, Krishna Reddy MC, Tarakaramu N, Ahmad H, Askar S, Abdullaev SS. Convective heat and mass transfer rate on 3D Williamson nanofluid flow via linear stretching sheet with thermal radiation and heat absorption. Sci Rep 2023;13:9889. [CrossRef]

[58] Akram N, Shah ST, Abdelrazek AH, Khan A, Kazi SN, Sadri R, et al. Application of PEG-Fe3O4 nanofluid in flat-plate solar collector: An experimental investigation. Sol Energy Mater Sol Cells 2023;263:112566. [CrossRef]

[59] Mostafizur RM, Rasul MG, Nabi MN, Haque R, Jahirul MI. Thermodynamic analysis of a flat plate solar collector with different hybrid nanofluids as working medium—A thermal modelling approach. Nanomaterials 2023;13:1320. [CrossRef]

[60] Memon S, Fang Y, Eames PC. The influence of low-temperature surface induction on evacuation, pump-out hole sealing and thermal performance of composite edge-sealed vacuum insulated glazing. Renew Energy 2019;135:450–464. [CrossRef]

[61] Zhang S, Kong M, Miao H, Memon S, Zhang Y, Liu S. Transient temperature and stress fields on bonding small glass pieces to solder glass by laser welding: Numerical modelling and experimental validation. Sol Energy 2020;209:350–362. [CrossRef]

[62] Henshall P, Eames P, Arya F, Hyde T, Moss R, Shire S. Constant temperature induced stresses in evacuated enclosures for high performance flat plate solar thermal collectors. Sol Energy 2016;127:250–261. [CrossRef]

[63] Arya F, Hyde T, Henshall P, Eames P, Moss R, Shire S, et al. Fabrication analysis of flat vacuum enclosures for solar collectors sealed with Cerasolzer 217. Sol Energy 2021;220:635–649. [CrossRef]

[64] Alawi OA, Kamar HM, Abdelrazek AH, Mallah AR, Mohammed HA, Abdulla AI, et al. Hydrothermal and energy analysis of flat plate solar collector using copper oxide nanomaterials with different morphologies: Economic performance. Sustain Energy Technol Assess 2022;49:101772. [CrossRef]

[65] Nabi H, Pourfallah M, Gholinia M, Jahanian O. Increasing heat transfer in flat plate solar collectors using various forms of turbulence-inducing elements and CNTs-CuO hybrid nanofluids. Case Stud Therm Eng 2022;33:101909. [CrossRef]

[66] Khetib Y, Alzaed A, Tahmasebi A, Sharifpur M, Cheraghian G. Influence of using innovative turbulators on the exergy and energy efficacy of flat plate solar collector with DWCNTs-TiO2/water nanofluid. Sustain Energy Technol Assess 2022;51:101855. [CrossRef]

[67] Akram N, Montazer E, Kazi SN, Soudagar MEM, Ahmed W, Zubir MNM, et al. Experimental investigations of the performance of a flat-plate solar collector using carbon and metal oxides based nanofluids. Energy 2021;227:120452. [CrossRef]

[68] Soudagar MEM, Nik-Ghazali NN, Kalam MA, Badruddin IA, Banapurmath NR, Ali MA, et al. An investigation on the influence of aluminium oxide nano-additive and honge oil methyl ester on engine performance, combustion and emission characteristics. Renew Energy 2020;146:2291–2307. [CrossRef]

[69] Holman JP. Experimental Methods for Engineers. 8th ed. New York: McGraw-Hill; 2021.

[70] Alotaibi S, Amooie MA, Ahmadi MH, Nabipour N, Chau KW. Modeling thermal conductivity of ethylene glycol-based nanofluids using multivariate adaptive regression splines and group method of data handling artificial neural network. Eng Appl Comput Fluid Mech 2020;14:379–390. [CrossRef]

[71] Wessel DJ. ASHRAE Fundamentals Handbook 2001 (SI edition). American Society of Heating, Refrigerating & Air Conditioning Engineers, Incorporated; 2001.

[72] Abu-Zeid MA, Elhenawy Y, Bassyouni M, Majozi T, Toderas M, Al-Qabandi OA, et al. Performance enhancement of flat-plate and parabolic trough solar collector using nanofluid for water heating application. Results Eng 2024;21:101673. [CrossRef]

[73] Kalbande VP, Choudhari MS, Nandanwar YN. Hybrid nano-fluid for solar collector based thermal energy storage and heat transmission systems: A review. J Energy Storage 2024;86:111243. [CrossRef]

[74] Kuwar M, Singh S, Ghosh SK, Singh RP. Thermal performance modelling of solar flat plate parallel tube collector using ANN. Energy 2024;131940. [CrossRef]

[75] Huminic G, Huminic A. Capabilities of advanced heat transfer fluids on the performance of flat plate solar collector. Energy Rep 2024;11:1945–1958. [CrossRef]

[76] Chilambarasan L, Thangarasu V, Ramasamy P. Solar flat plate collector's heat transfer enhancement using grooved tube configuration with alumina nanofluids: Prediction of outcomes through artificial neural network modeling. Energy 2024;289:129953. [CrossRef]

[77] Abduljleel MA, Yasin NJ, Ghadhban SA, Soomro SA. Performance improving for the flat plate solar collectors by using nanofluids: Review study. J Tech 2024;6:1891. [CrossRef]

[78] Hussein AM, Awad AT, Ali HHM. Evaluation of the thermal efficiency of nanofluid flows in flat plate solar collector. J Therm Eng 2024;10:299–307. [CrossRef]

[79] Bhargva M, Kumar P, Sharma M, Batra NK, Behl RK. A novel methodology of literature review of a flat plate liquid solar collector. J Sol Energy Res 2024;9:1822–1842.

[80] Jyani L, Sharma S, Chaudhary K, Purohit K. Direct absorption solar collector: An experimental investigation of Al2O3-H2O nanofluid over the flat plate at different tilt angles and mass-flow rates. New Energy Exploit Appl 2024;3:24–40. [CrossRef]

[81] Khan F, Karimi MN, Khan O, Yadav AK, Alhodaib A, Gürel AE, et al. A hybrid MCDM optimization for utilization of novel set of biosynthesized nanofluids on thermal performance for solar thermal collectors. Int J Thermofluids 2024;22:100686. [CrossRef]

[82] Sreekumar S, Shaji J, Cherian G, Thomas S, Mondol JD, Shah N. Corrosion analysis and performance investigation of hybrid MXene/C-dot nanofluid-based direct absorption solar collector. Sol Energy 2024;269:112317. [CrossRef]

[83] Ajeena AM, Farkas I, Víg P. Energy and exergy assessment of a flat plate solar thermal collector by examining silicon carbide nanofluid: An experimental study for sustainable energy. Appl Therm Eng 2024;236:121844. [CrossRef]